

Strong Coupling between Microwave Photons and Nanomagnet Magnons

by

Justin T. Hou

Submitted to the Department of Electrical Engineering and Computer
Science

in partial fulfillment of the requirements for the degree of

Master of Science in Electrical Engineering and Computer Science

at the

MASSACHUSETTS INSTITUTE OF TECHNOLOGY

September 2019

© Massachusetts Institute of Technology 2019. All rights reserved.

Signature redacted

Author

Department of Electrical Engineering and Computer Science

August 30, 2019

Signature redacted

Certified by

Luqiao Liu

Associate Professor of Electrical Engineering and Computer Science

Thesis Supervisor

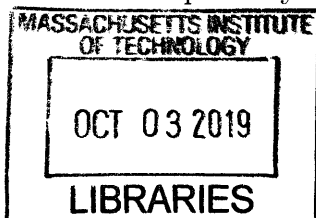
Signature redacted

Accepted by

Leslie A. Kolodziejski

Professor of Electrical Engineering and Computer Science

Chairman, Department Committee on Graduate Students



ARCHIVES

Strong Coupling between Microwave Photons and Nanomagnet Magnons

by

Justin T. Hou

Submitted to the Department of Electrical Engineering and Computer Science
on August 30, 2019, in partial fulfillment of the
requirements for the degree of
Master of Science in Electrical Engineering and Computer Science

Abstract

Coupled microwave photon-magnon hybrid systems offer promising applications by harnessing various magnon physics. At present, in order to realize high coupling strength between the two subsystems, bulky ferromagnetic insulators with large spin numbers are utilized, which limit their potential applications for scalable quantum information processing.

In this thesis, by enhancing single spin coupling strength using lithographically defined superconducting resonators, we demonstrate high cooperativities between a resonator mode and a Kittel mode in nanometer thick Permalloy wires. Strong magnon-photon coupling is achieved with number of spins in the order of 10^{13} , three orders of magnitude lower compared with previous studies. Moreover, we confirm the scaling law of coupling strength as a function of spin numbers. The experimental single spin-photon coupling strengths are extracted, which attain reasonable agreement with values derived from our quantum mechanical model. Our model therefore provides a guideline for further scaling down of the magnonic volume, which indicates that the number of spins for reaching strong coupling can be reduced to 10^4 with optimized material and resonator design. The realization of the coupled systems using metallic ferromagnets with conventional Si-substrates demonstrates a highly engineerable and industrial compatible on-chip device design, which opens up the possibility to investigate magnon-photon coupling in a wide range of spintronic devices, such as magnetic tunnel junctions. Our results provide a novel platform of magnon-photon coupled systems, where the interplay of spintronics, light-matter interaction, and quantum information science can be studied in an on-chip and lithographically scalable architecture.

Thesis Supervisor: Luqiao Liu

Title: Associate Professor of Electrical Engineering and Computer Science

Acknowledgments

It is my great pleasure to be accepted by MIT EECS and work in Prof. Luqiao Liu's group. As a student who majored in both EE and Physics in undergraduate, I have always been searching for a research field which applies interesting physics to engineering applications. I am lucky to meet Prof. Liu and the field of spintronics. I would like to thank my thesis supervisor, Prof. Liu, for kind and patient guidance of my research projects. From Prof. Liu, I have learned a great deal from experimental details, manuscript preparation, conference presentation, to defining meaningful research directions.

I would also like to thank my labmates, Jiahao Han, Pengxiang Zhang, Taqiyyah Safi, Joseph Finley, Hailong Wang, Yanfei Wu, Hexin Zhou, and Saima A. Siddiqui for their kind help on experiments and discussions about the field of spintronics. I really learned a lot from my friendly and talented labmates. They provided me with a supportive environment and I really had a great time working with them.

I would like to thank MTL staffs for supporting my researches during this period of time. I would like to thank Kurt Broderick, Gary Riggot, and Dennis Ward for teaching me several fabrication facilities. Without their guidance and suggestions, I would not be able to complete this thesis. I would also like to thank our assistant Steven O'Hearn for handling several lab purchases for us, which allows me to concentrate more on research projects. I would like to also thank Mark Belanger for teaching me machine shop facilities. With his help and guidance, I am able to design and make tools for our measurement systems.

Finally, I would like to thank my parents with deepest love. Conducting research is not always successful, but most of the time frustrating. However, my parents always give me warm mental support to help me deal with stress and frustration. They always support me to pursue what I love, which encourage me to overcome obstacles in my academic career.

Contents

1	Introduction	15
1.1	Cavity Quantum Electrodynamics	16
1.2	Circuit Quantum Electrodynamics and Hybrid Quantum Systems . .	20
1.3	Magnon-Photon Coupled Systems	24
1.4	Spintronic effects for magnetic dynamics	26
1.5	Outline of the thesis	28
2	Theory of Magnon-Photon Coupled Systems using Superconducting Resonators	29
2.1	Coplanar waveguide (CPW) as a transmission line	29
2.2	CPW resonators and lumped element (LE) resonators	31
2.3	Quantization of superconducting resonators as LC circuits	32
2.4	Theoretical description of ferromagnetic resonance magnon modes . .	34
2.5	Magnon-photon coupled systems with LC circuits	36
3	Experimental Setups	41
3.1	Material and device design	41
3.2	Device fabrication	43
3.3	Measurement setup and procedure	44
4	Experiments of Magnon-Photon Coupled Systems using Superconducting Resonators	47
4.1	Simulation and characterization of CPW resonators	47

4.2	Magnon-photon coupled systems using CPW resonators	49
4.3	Simulation and characterization of LE resonators	51
4.4	Magnon-photon coupled systems using LE resonators	53
4.5	Extraction of single spin-photon coupling strength	54
5	Conclusions	57

List of Figures

1-1	A schematic illustration of Cavity QED. An atom as a two-level system is passed through a cavity over a transit time $t_{transit}$. In the cavity, the atom interacts with photon modes through coupling strength g using electric dipole interaction. The cavity and atom decay rates are κ and γ , respectively.	16
1-2	a) Illustration of basis states in Janes-Cummings model. b) The energy level alignment of dressed states in the case of on-resonance ($\Omega = \omega_c$).	17
1-3	Illustration of Rabi oscillation between $ 0, e\rangle$ and $ 1, g\rangle$ in the case of on-resonance. The loss of the system is assumed to be zero in this plot.	19
1-4	The dispersive shift of resonant frequency of a cavity, which is qubit state dependent. This mechanism can be used for qubit readout.	20
1-5	A schematic illustration of Circuit QED. 1D CPW resonator is used for cavity system and superconducting qubit is utilized as an artificial atom. Qubit is placed at voltage antinode for maximum electric dipole interaction. The system is on-chip and scalable.	21
1-6	a) An LC circuit is SHO with equal energy spacing. b) By replacing inductor using a Josephson junction, the lowest two states define a two-level system due to nonlinearity induced anharmonicity.	22
1-7	Hybrid quantum systems combine different physical systems, affording advantages that cannot be gained from a single system alone, and thus have promise for the development of future quantum technologies.	23

1-8	An illustration of magnon-photon coupled system. Inside a 3D cavity, a mm-sized YIG sphere is coupled with microwave photon modes through magnetic dipole interaction.	24
1-9	a) Spin-Transfer Torque (STT) through spin-filtering in a magnetic tunnel junction (MTJ). The charge current J_e passing through first magnetic layer \mathbf{m}_1 becomes spin-polarized, and exert STT on the second magnetic layer \mathbf{m}_2 . b) Spin-Orbit Torque (SOT) through Spin-Hall Effect (SHE) in a heavy metal/ferromagnetic metal bilayer. The charge current \mathbf{J}_e generates spin accumulation ($-\sigma$) which is perpendicular to the current direction at the interface and exerts a SOT on the magnetic moments. The damping-like SOT is proportional to $\mathbf{m} \times (\sigma \times \mathbf{m})$ and can be described by an effective field $\mathbf{H}_{DL} \sim \sigma \times \mathbf{m}$. Here, only the damping-like term is presented.	27
3-1	a) A PCB with a CPW resonator device. The signal line and the ground of the resonator device are wired-bonded to the signal line and the ground of the PCB, respectively. Note that several wires are bonded to ensure good microwave transmission. b) The PCB is mounted to the sample holder with screws to ensure thermal contact. The SMA connectors on the PCB are connected to RF coaxial cables.	44
3-2	a) The Janis 1.5 K cryostat with a magnet setup at the bottom. b) Cryostat with the sample rod inserted. The sample rod consists of feedthrough for external RF cable connection. c) The Vector Network Analyzer (VNA) for microwave transmission measurement.	45
4-1	Photo of a CPW resonator device with $100\mu\text{m} \times 8\mu\text{m} \times 50\text{nm}$ MgO/Py/Pt stripe deposited at the center of the signal line. The distance $l = 12$ mm between the two open gaps at the ends of CPW defines the fundamental resonant frequency to be 4.96 GHz.	48

4-2	a) Microwave transmission simulated using Sonnet. Lossless conductor with zero thickness is assumed for the superconducting Nb structure.	
	b) Microwave transmissions at 1.5 K with zero applied field before and after Py is deposited, exhibiting resonance signals with quality factors 1570 and 760, respectively. With Py, the resonator mode is blue detuned due to residual coupling to the magnon mode.	48
4-3	a) Microwave transmission as a function of frequency and in-plane magnetic field at 1.5 K for a sample with $500\mu\text{m}\times 8\mu\text{m}\times 50\text{nm}$ Py showing characteristic anti-crossing of magnon-photon coupling. b) Theoretical microwave transmission spectrum calculated using input-output theory with parameters obtained from the experiment.	49
4-4	Image of a low-impedance lumped element resonator device with $40\mu\text{m}\times 2\mu\text{m}\times 10\text{nm}$ MgO/Py/Ta stripe deposited at the center of the $4\mu\text{m}$ wide inductive wire.	51
4-5	Left: Microwave transmission of the low-impedance resonator obtained from experiment and simulation. Two modes are observed as transmission minima due to photon absorption from the signal line. Right: Simulation of current density distribution of the resonant modes, respectively. Red and blue color indicates regions with strong and weak current densities, respectively. The first harmonic mode exhibits large current density at the central inductive wire which enhances coupling.	52
4-6	Microwave transmission as a function of frequency and in-plane magnetic field at 1.5 K. $\mu_0 M_s = 1.1\text{ T}$ and $g/2\pi = 74.5\text{ MHz}$ are determined from the fitting shown in dashed line. Minimum transmission shows up under resonant conditions.	53
4-7	Magnon-photon coupling strength g as a function of magnetic volume and spin number. The dashed lines represent fittings of the scaling rule $g = g_s\sqrt{N}$. The single spin coupling strength for two resonators in this work are determined to be $g_s^{\text{CPW}}/2\pi = 18\text{ Hz}$ and $g_s^{\text{LE}}/2\pi = 263\text{ Hz}$ in CPW resonators and lumped element resonators, respectively. .	55

5-1 We developed the "Circuit QED version" of magnon-photon coupled systems, which provides potential applications to Hybrid Quantum Systems with magnon physics and spintronic effects. 58

List of Tables

4.1	Table for different CPW resonators with Py 50 nm thick deposited. .	51
4.2	Table for different lumped element resonators with Py 10 nm thick deposited.	54

Chapter 1

Introduction

The advancement of modern technology has benefited from the understanding of fundamental physics. The most prominent example is the development of semiconductor and solid state physics, which lay the foundation of modern electronic devices. Besides physics, the ability to fabricate devices and ultimately to integrate them in a highly controllable manner using lithography process is the key to building integrated circuits and computing chips. Therefore, a physical platform which holds novel physics and fabrication scalability has high potential for both fundamental researches and engineering applications.

In this thesis, we realize such a platform: a lithographically scalable architecture of magnon-photon coupled systems. The magnon-photon coupled system has recently attracted great attention by placing ferrimagnetic yttrium iron garnet (YIG) in a resonant cavity. Here we demonstrate its compatibility with semiconductor fabrication process and one of the leading quantum computing architecture, Circuit Quantum Electrodynamics (Circuit QED). In this introduction, we will first provide an introduction of Cavity Quantum Electrodynamics (Cavity QED), where some physics are shared by magnon-photon coupled systems and Circuit QED. Next, we briefly review Circuit QED and Hybrid Quantum Systems to appreciate potential applications to quantum information science. We will also review recent development of magnon-photon coupled systems. Finally, we discuss how spintronic effects can potentially be utilized for active sensing and control of this coupled system in our architecture.

1.1 Cavity Quantum Electrodynamics

Cavity QED studies the interaction between atoms and photons in a three dimensional resonant cavity, where the quantum nature of photons becomes important (Fig. 1-1). Because of the pioneering studies of light-matter interaction using Cavity QED, Serge Haroche [30] and David Wineland [72] were awarded Nobel Prize in Physics in 2012. The physics of Cavity QED are similarly shared by Circuit QED, a platform for realizing commercial quantum computers, which we will introduce in the next section. Moreover, the analogy of physics is also explored in magnon-photon coupled system, which is the main focus of our thesis.

In free space, it is known that atoms in excited states will spontaneously decay and emit photons. The decay rate is proportional to the photon density of states at energy corresponding to atomic energy level splitting. However, inside a cavity, only photons with specific energy and wavelength are allowed, and the photon density of states are modified accordingly. Therefore, the spontaneous emission behaviors of atoms are also dramatically changed. The spontaneous decay rate of an atom can be enhanced if the transition frequency is on resonance with one of the photon modes[24], and it can also

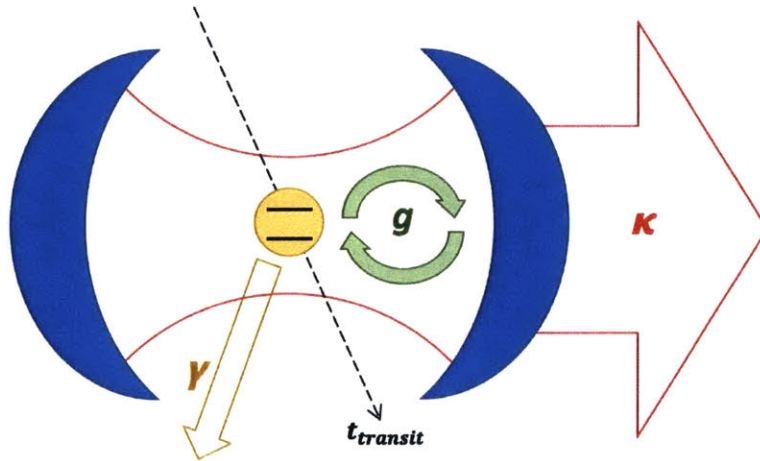


Figure 1-1: A schematic illustration of Cavity QED. An atom as a two-level system is passed through a cavity over a transit time $t_{transit}$. In the cavity, the atom interacts with photon modes through coupling strength g using electric dipole interaction. The cavity and atom decay rates are κ and γ , respectively.

be suppressed in the condition of off-resonance [38]. Besides change of decay rates, when the atom-photon coupling strength is larger than their individual decay rates, strong coupling regime is achieved. In this situation, an atom is able to reabsorb the spontaneously emitted photon, and the energy can be coherently transferred between the atom and the photon states, a phenomena called Rabi oscillations [15]. The ability to transfer quantum excitation between the two systems signifies the possibility to realize quantum computation.

To provide a qualitative description, the Hamiltonian of the atom-photon coupled system can be effectively described by the coupling of an atomic two-level system with a simple harmonic oscillator (SHO), called the Janes-Cummings model [11]:

$$\begin{aligned}\hat{H} &= \hat{H}_{SHO} + \hat{H}_{two-level} + \hat{H}_{int} \\ &= \hbar\omega_c \left(a^\dagger a + \frac{1}{2} \right) + \frac{\hbar\Omega}{2} \sigma^z + \hbar g (a^\dagger \sigma^- + a \sigma^+)\end{aligned}\quad (1.1)$$

where ω_c , Ω , and g describe the cavity resonant frequency, the atomic level splitting, and the atom-photon coupling strength, respectively. The operator a (a^\dagger) is the cavity photon annihilation (creation) operator and the Pauli matrices (σ^z, σ^+ , and σ^-) are the operators for the two-level system. In general, the SHO Hamiltonian can include more than one mode due to the multimode nature of the cavity. Here we assume that

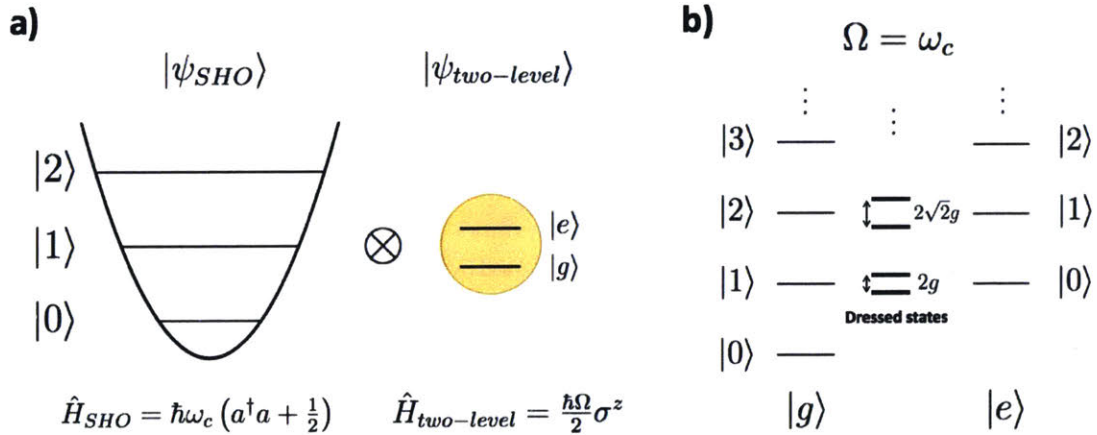


Figure 1-2: **a)** Illustration of basis states in Janes-Cummings model. **b)** The energy level alignment of dressed states in the case of on-resonance ($\Omega = \omega_c$).

only a single photon mode is near resonance with the atomic states, and therefore the inclusion of a single mode is sufficient to describe the physics of atom-photon coupling. $|0\rangle |1\rangle |2\rangle |3\rangle$ In this model, the basis states of the Hilbert space can be written as $|\psi_{SHO}\rangle \otimes |\psi_{two-level}\rangle \equiv |\psi_{SHO, \psi_{two-level}}\rangle$, where we will write $|\psi_{SHO}\rangle = |n\rangle$ to denote SHO state with n energy quanta, and $|\psi_{two-level}\rangle = |e\rangle$ or $|g\rangle$ to denote excited or ground state of the two-level system (Fig. 1-2a). Note that the basis states are the eigenstates of both \hat{H}_{SHO} and $\hat{H}_{two-level}$. Moreover, the interaction \hat{H}_{int} only induces coupling between $|n, e\rangle$ and $|n+1, g\rangle$ for a given n . It is therefore possible to directly diagonalize the Hamiltonian in the subspace of $|n, e\rangle$ and $|n+1, g\rangle$. The resulting excited eigenstates are called dressed states [11]:

$$\begin{aligned} |n, +\rangle &= \cos \theta_n |n, e\rangle + \sin \theta_n |n+1, g\rangle \\ |n, -\rangle &= -\sin \theta_n |n, e\rangle + \cos \theta_n |n+1, g\rangle \end{aligned} \tag{1.2}$$

where the corresponding energies are $E_{n,\pm} = \hbar\omega_c(n+1) \pm \frac{\hbar}{2}\sqrt{4g^2(n+1) + \Delta^2}$, and $\theta_n = \frac{1}{2} \tan^{-1} \left(\frac{2g\sqrt{n+1}}{\Delta} \right)$, with $\Delta = \Omega - \omega_c$ being the atom-cavity photon detuning. Note that the lowest energy basis state $|n=0, g\rangle$ does not couple to other states, and therefore it is the ground state of the system with ground state energy $E_{0,g} = -\frac{\hbar\Omega}{2}$.

The resulting energy spectrum can be analyzed in the cases of on-resonance ($\Delta = 0$) and dispersive regime ($g/\Delta \ll 1$). In the case of on-resonance (Fig. 1-2b), the basis states $|n, e\rangle$ and $|n+1, g\rangle$ have the same energy, but the atom-photon interaction resulting in dressed states $|n, \pm\rangle$ with energy splitting $2\hbar g\sqrt{n+1}$. This energy level splitting can be observed in spectroscopy if the splitting is larger than the combined linewidths of photon and atom [31]. Moreover, with the interaction, the basis states are no longer the energy eigenstates (or, stationary states). Therefore, in the time domain, an initial state with an excited atom and zero photon $|0, e\rangle$ will be transformed into $|1, g\rangle$ and back again with vacuum Rabi frequency g/π (Fig. 1-3). This is the realization of Rabi oscillation. In the dispersive regime, after a suitable unitary transformation $U = \exp \left[\frac{g}{\Delta} (a\sigma^+ - a^\dagger\sigma^-) \right]$, the Hamiltonian can be effectively

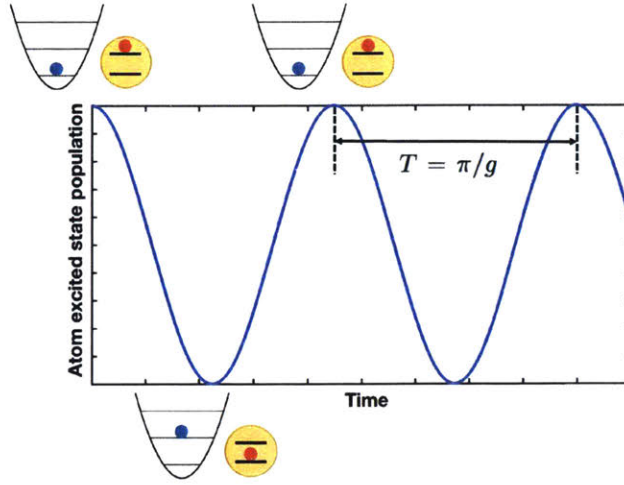


Figure 1-3: Illustration of Rabi oscillation between $|0, e\rangle$ and $|1, g\rangle$ in the case of on-resonance. The loss of the system is assumed to be zero in this plot.

written as $\omega_{01} \neq \omega_{12} 1/\sqrt{LC}$:

$$H \approx \hbar\omega_c \left(a^\dagger a + \frac{1}{2} \right) + \frac{\hbar\Omega}{2} \sigma^z + \hbar \frac{g^2}{\Delta} \left(a^\dagger a + \frac{1}{2} \right) \sigma^z$$

The first two terms are the original $\hat{H}_{SHO} + \hat{H}_{two-level}$. The last term is the effective interaction in the dispersive regime, which can be viewed either as an atom-state-dependent cavity frequency shift or as a photon-number-dependent atom frequency shift (ac Stark plus Lamb shifts) [14, 60, 52]. With this interaction, it is possible to probe the atomic quantum state based on the measurement of the cavity resonant frequency. In other words, the resonator frequency can take the two values $\omega_c \pm g^2/\Delta$ depending on the qubit state. This dispersive shift of cavity frequency is used in Circuit QED for readout of qubit states [11] (Fig. 1-4).

The pioneering works of Cavity QED have demonstrated several important physics of atom-cavity coupled systems. Some of the physics, such as energy level splitting, Rabi oscillations, and ac Stark shifts, are also similarly shared in magnon-photon coupled systems. In Cavity QED, the atom couples with the photon mode through electric dipole interaction. Therefore, atomic states with large electric dipole moment, called Rydberg states [1, 13, 15, 57], are often utilized for reaching large coupling

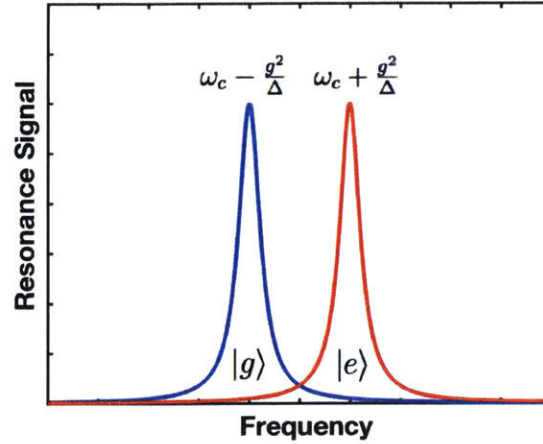


Figure 1-4: The dispersive shift of resonant frequency of a cavity, which is qubit state dependent. This mechanism can be used for qubit readout.

strength.

1.2 Circuit Quantum Electrodynamics and Hybrid Quantum Systems

The field of Circuit Quantum Electrodynamics (Circuit QED) followed the ideas of Cavity QED, while planar superconducting resonators are utilized for photon modes, and superconducting qubits serve as artificial atoms [69, 11] (Fig. 1-5). In this architecture, the high quality factor superconducting resonator is a one-dimensional coplanar waveguide (CPW) resonator. A CPW resonator is formed by creating open gaps at the two ends of signal line in a CPW, where current nodes (and voltage antinodes) are defined. Compared with the 3D cavities utilized in Cavity QED, the other two dimensions which do not define the resonant frequency are spatially minimized, and therefore the effective mode volume of the resonant mode is greatly reduced, resulting in enhanced energy density for higher coupling strength. The photon modes in a superconducting resonator can be described by an LC circuit, a realization of SHO, which we will treat theoretically in the next chapter. By replacing the inductor in an LC circuit with a nonlinear inductor, a superconducting qubit is

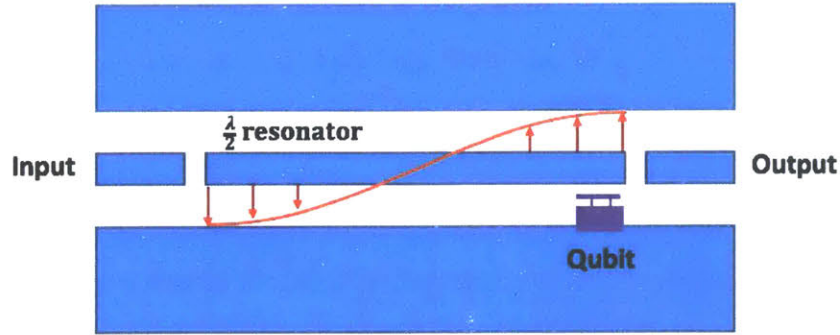


Figure 1-5: A schematic illustration of Circuit QED. 1D CPW resonator is used for cavity system and superconducting qubit is utilized as an artificial atom. Qubit is placed at voltage antinode for maximum electric dipole interaction. The system is on-chip and scalable.

formed (This type of qubit is called Cooper pair box) [11]. The nonlinearity changes the equal spacing of energy levels in SHO and the resulting lowest two energy levels can be effectively modeled as a two-level system (Fig. 1-6). Such a dissipationless nonlinear inductor can be realized by a Josephson junction, which consists of two superconducting electrodes separated by a thin insulating barrier ($\sim 1\text{nm}$). To reach large coupling strength with electric dipole interaction, one can put the qubit at the voltage antinode of the CPW resonator mode.

All of the physics mentioned in previous discussion of Cavity QED can be realized in Circuit QED. Compared with Cavity QED, the small mode volume of the resonator photon modes and the large dipole moment of superconducting qubits due to their macroscopic sizes are ideal for reaching strong (or even ultrastrong) coupling regime [21]. Moreover, the systems in Circuit QED can be fabricated using semiconductor lithography process. Therefore, it is possible to precisely fabricate an integrated system with multiple resonators and qubits on a chip, where different parts of the system can be interconnected using superconducting circuits [35]. In this sense, Circuit QED is a scalable architecture for solid state quantum computation. Single qubit gates can be realized by applying microwave drives to the resonator, and qubit state readout is achieved by measuring dispersive shift in resonator transmission spectrum. Moreover, two-qubit gates can be realized by coupling two qubits with a superconducting

quantum bus.

The lithographically scalable architecture and its compatibility with microwave electronics have set Circuit QED as one of the leading technologies for realizing integrated quantum computing systems [59, 71]. Recent important progress includes high measurement and gate fidelities which surpass the threshold required by 2D surface code for fault-tolerant quantum computation [8], and the experimental demonstration of 1D repetition code for the validation of quantum error correction protocols [36]. Moreover, systems with more than 50 qubits have been built, with the goal for achieving quantum supremacy: the experimental demonstration of a quantum algorithm which surpasses the capabilities of any classical computer [12, 51].

Despite recent important experimental demonstrations, there are limitations of superconducting qubits. For example, the qubit coherence time is in the order of 10-100 μs at milli-Kelvin cryogenic temperature, while other systems such as electron spins or nuclear spins are demonstrated to have seconds or minutes coherence time even in room temperature. Therefore, it is proposed to combine the fast processing

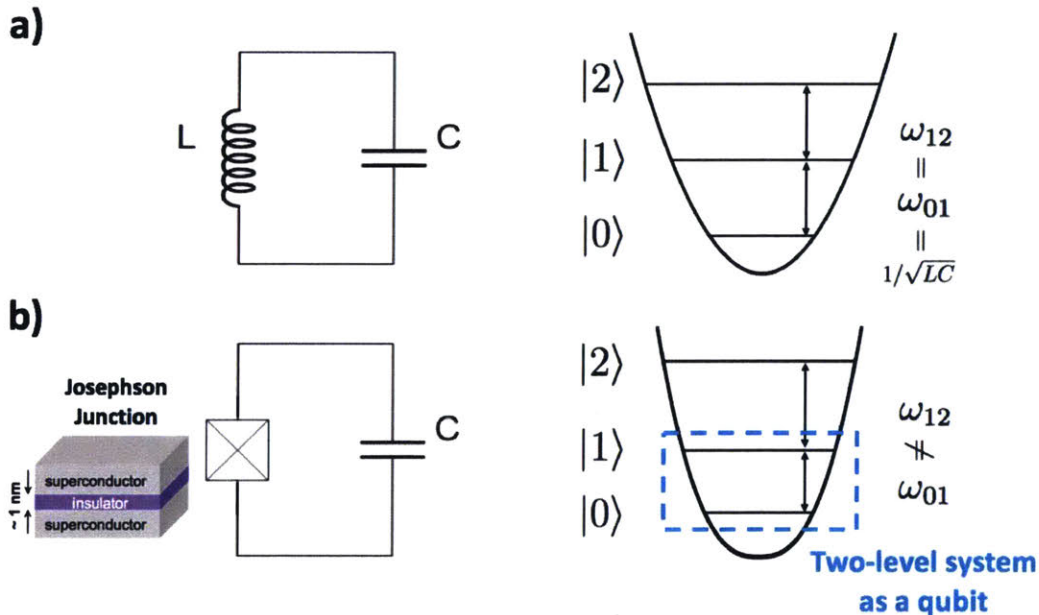


Figure 1-6: **a)** An LC circuit is SHO with equal energy spacing. **b)** By replacing inductor using a Josephson junction, the lowest two states define a two-level system due to nonlinearity induced anharmonicity.

speed of superconducting qubits with long-lived spins as quantum memories [56, 34, 73, 61, 3, 39, 78, 25]. Besides quantum information processing and storage, in the more general context of quantum information science, transmission of quantum information may lead to practical quantum cryptography [22]. However, quantum cryptography is mostly achieved using optical photons propagating in free space or optical fibers, instead of microwave photons in superconducting quantum computation. Therefore, a coherent microwave-to-optics quantum transducer is required, which is actively pursued in nano-mechanical oscillator systems [63, 6]. The requirement of systems which can simultaneously perform different tasks calls for a new architecture: the idea of Hybrid Quantum Systems (HQS), which can harness advantages of distinct physical systems and realize functions that cannot be achieved with any individual sub-system alone [74, 41].

Besides superconducting qubits, spin ensembles, and nano-mechanical oscillators, the realm of HQS is actively explored in other quantum systems, such as ions, atoms [16], molecules [5], and spins in quantum dots [54, 68, 48]. In HQS, electric dipole interactions have been traditionally utilized to couple photons with other quantum excitations. Systems with magnetic dipole interaction, such as spin ensembles, utilize

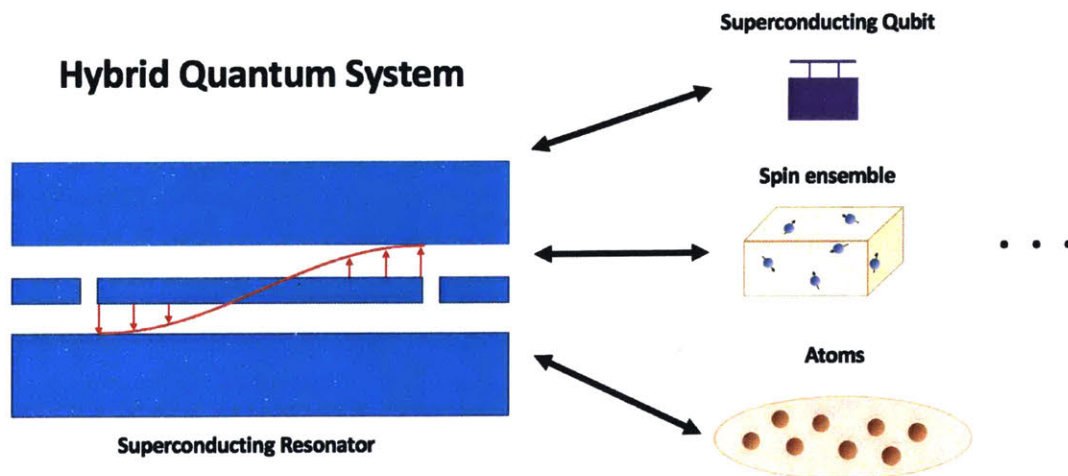


Figure 1-7: Hybrid quantum systems combine different physical systems, affording advantages that cannot be gained from a single system alone, and thus have promise for the development of future quantum technologies..

the collective enhancement of coupling strength with spin number ($g = g_s\sqrt{N}$) to overcome the weak single spin-photon coupling strength g_s . By far, the most successful demonstration of HQS utilizes superconducting circuits as a "microwave quantum bus" as an interface between different quantum systems. Therefore, it is of great importance to expand the family of quantum systems in HQS which are also compatible with superconducting circuits, namely, Circuit QED compatible [74].

1.3 Magnon-Photon Coupled Systems

Magnon-photon coupled systems have recently attracted great attention as an alternative system to study light-matter interaction using magnetic dipole coupling [62, 32, 76, 64, 23, 7, 49]. In this system, magnons in magnetic materials with high spin density are utilized, where coupling strength g is collectively enhanced by square root of number of spins ($g = g_s\sqrt{N}$) [64] to overcome the weak coupling strength g_s between individual spins and the microwave field. Along this line, sizable ferrimagnets, yttrium iron garnet (YIG) with millimeter dimensions have been employed for reaching strong coupling (Fig. 1-8)

Recent important demonstrations include the realization of strong coupling and

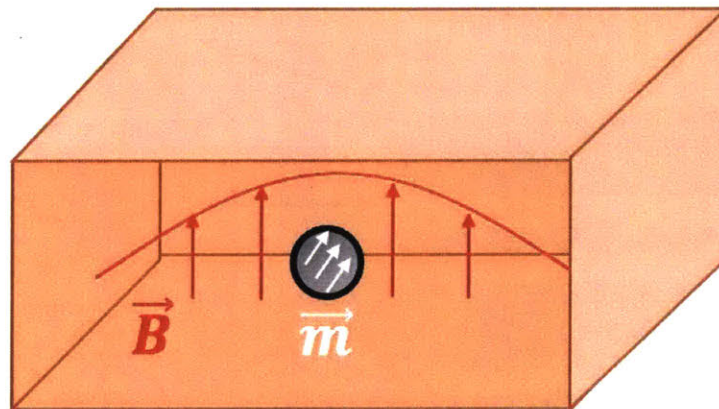


Figure 1-8: An illustration of magnon-photon coupled system. Inside a 3D cavity, a mm-sized YIG sphere is coupled with microwave photon modes through magnetic dipole interaction.

Rabi-like oscillations in both room temperature and cryogenic temperature [76, 49], nonlinear effects induced by magnons [70], non-Hermitian physics and the observation of exceptional points [75, 29], and various coupling spectrums including Purcell effect, magnetically induced transparency [76], and even level-attraction [28]. These pioneering results demonstrate the rich physics of magnon-photon coupled systems. In particular, level-attraction is rarely found in other light-matter interaction systems, whose microscopic physical origin is still under debate [55]. Besides, the quantum nature of magnons are also explored. Magnon-qubit coupling mediated by 3D cavity photons is demonstrated [65], which is utilized to resolve magnon number states in the dispersive regime [42]. The change of magnetic moment corresponding to single spin flip among more than 10^{19} spins in the magnet is detected. Moreover, magnon-gradient memory is studied using multiple YIG spheres in a 3D cavity, where the magnon-dark mode is effectively decoupled from the cavity for a long storage lifetime, demonstrating the potential for quantum memory applications [77].

While great success has been demonstrated in achieving coherent sensing and control over the magnonic quantum state using this architecture [65, 77, 42], one important question remains unanswered: whether such a system is scalable for achieving integrated hybrid quantum systems. In the meantime, reducing the size of magnets in this hybrid quantum system can potentially provide another degree of freedom for realizing active sensing and control of quantum states: In the study of spin electronics, sophisticated techniques have been developed for manipulating and detecting spin states using various electrical methods, however these effects only work efficiently in nanoscale magnets [37, 4, 18, 47, 19]. Therefore, a magnon-photon coupled system with scalability, Circuit QED compatibility, and high coupling strength with nanomagnets remains to be demonstrated, which will hold promising applications to hybrid quantum systems by incorporating magnon physics and spintronic effects.

1.4 Spintronic effects for magnetic dynamics

In the field of spintronics, researchers have demonstrated the manipulation of magnetic moments in magnetic materials by injection of spin-polarized electrons. The injected spins (σ) can transfer their spin angular momentum to the magnetic moments (\mathbf{m}) in a ferromagnet, thereby exerting a spin-torque. The spin-torques can be decomposed into field-like torques ($\tau_{FL} \sim \mathbf{m} \times \sigma$) and damping-like torques ($\tau_{DL} \sim \mathbf{m} \times (\sigma \times \mathbf{m})$) [44], which can be described using effective magnetic field $\mathbf{H}_{FL} \sim \sigma$ and $\mathbf{H}_{DL} \sim \sigma \times \mathbf{m}$. The spin-polarized current can be generated using spin-filtering effect, by passing a current through a ferromagnetic (FM) "polarizer" layer in the structure of metallic spin valves (FM/normal metal/FM) or magnetic tunnel junctions (FM/oxide/FM) [58, 40]. This mechanism is called Spin-Transfer Torque (STT) (Fig. 1-9a). Beside, spin current can also be generated by a charge current using Spin-Hall Effect (SHE) (or Rashba Effect [43]) in materials (or interfaces) with large spin-orbit coupling, where electrons with opposite spins are transversely deflected in opposite directions. This mechanism is called Spin-Orbit Torque (SOT) (Fig. 1-9b). Magnetic switching using either STT or SOT has been demonstrated [46], which signifies their applications to magnetic random access memory (MRAM). Besides spin torques which utilize charge currents, a finite voltage can greatly modify the magnetic anisotropy at the ferromagnet/oxide interface, in the absence of charge current. Such mechanism is called voltage-controlled magnetic anisotropy (VCMA) [2], which can be used to induce or assist magnetic switching.

In radio-frequency (RF) applications and magnetic dynamics, a DC spin-torque can actively adjust the damping of the ferromagnetic resonance (FMR) magnon modes [4], or even induce magnetic self-oscillations without external microwave drives [37, 18, 47, 19]. Moreover, an RF spin-torque can also induce FMR, which is called spin torque ferromagnetic resonance (ST-FMR) [45]. Besides, the VCMA can be utilized to control the FMR frequency using electric field instead of solely based on external magnetic field, which will have great advantage when superconductivity is involved in the system. All of these effects will allow active control of magnon-photon coupled

systems using spintronic effects. However, they are yet to be demonstrated due to the sizable ferrimagnetic insulating YIG used in previous studies.

Besides active control of magnetic dynamics, spintronic effects offer detection and sensing of magnetic dynamics. Spin-pumping is an effect where the dynamics of a ferromagnet will pump spin currents to an adjacent normal metal (NM) layer [66, 67]. In the case where NM is a heavy metal, the pumped spin current can be converted to a measurable voltage through Inverse Spin-Hall Effect (ISHE) [50]. The spin-pumping effect does not require miniaturized magnets, and therefore it has been successfully incorporated with magnon-photon coupled systems to investigate peculiar lineshapes of the coupled systems [7].

Clearly, reaching high magnon-photon coupling strength with nanomagnets will open up the utilization of spintronic effects for active sensing and control of the hybrid quantum systems.

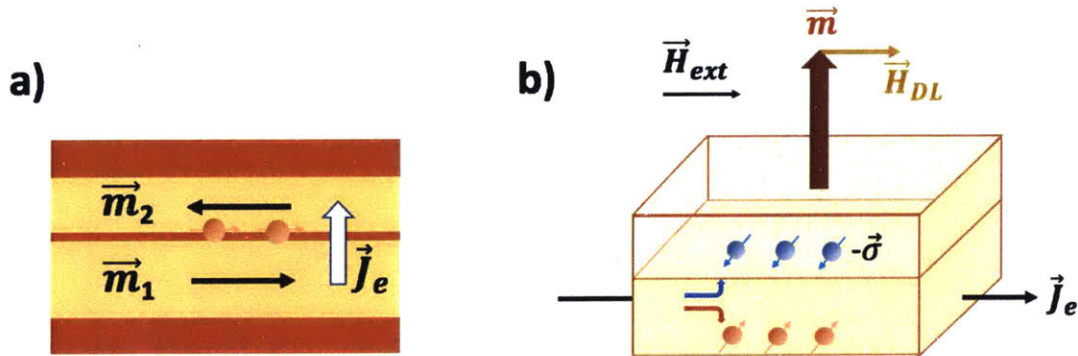


Figure 1-9: **a)** Spin-Transfer Torque (STT) through spin-filtering in a magnetic tunnel junction (MTJ). The charge current J_e passing through first magnetic layer \mathbf{m}_1 becomes spin-polarized, and exert STT on the second magnetic layer \mathbf{m}_2 . **b)** Spin-Orbit Torque (SOT) through Spin-Hall Effect (SHE) in a heavy metal/ferromagnetic metal bilayer. The charge current \mathbf{J}_e generates spin accumulation ($-\sigma$) which is perpendicular to the current direction at the interface and exerts a SOT on the magnetic moments. The damping-like SOT is proportional to $\mathbf{m} \times (\sigma \times \mathbf{m})$ and can be described by an effective field $\mathbf{H}_{DL} \sim \sigma \times \mathbf{m}$. Here, only the damping-like term is presented.

1.5 Outline of the thesis

In this thesis, by utilizing superconducting resonators, we demonstrate strong magnon-photon coupling with nanometer size Permalloy thin film stripe (Permalloy=Py=NiFe). Our on-chip, lithographically scalable, and Circuit QED compatible design provides a direct route towards realizing hybrid quantum systems with nanomagnets, whose coupling strength can be precisely engineered and dynamic properties can be controlled by various mechanisms derived from spintronic studies. In Chapter 2, we will discuss the theoretical aspects of magnon-photon coupled systems using superconducting resonators. In Chapter 3, we will introduce our experimental design and setups. In Chapter 4, we present our experimental results where the theoretical results from Chapter 2 are used for analysis. Finally in Chapter 5, we summarize our results with conclusions and outlook.

Chapter 2

Theory of Magnon-Photon Coupled Systems using Superconducting Resonators

In this Chapter, we will discuss the theoretical aspects of magnon-photon coupled systems. Particularly, we will provide quantum mechanical models for photon modes in superconducting resonators and magnon modes in ferromagnetic resonance. These results will be combined to derive the magnon-photon coupling strength and modes evolution, which have direct experimental consequences as will be shown in the next Chapter.

2.1 Coplanar waveguide (CPW) as a transmission line

A coplanar waveguide (CPW) is a realization of a transmission line [26]. The transmission line model describes the electromagnetic (EM) wave propagation in a distributed circuit, where wavelengths are comparable to the size of the circuit, in contrast to lumped element circuits in circuit theory. Transmission lines have important applications in RF engineering and can be physically realized by coaxial cables, striplines,

microstrips, or CPWs discussed here. In general, the voltage $V(x, t)$ and current $I(x, t)$ in a lossless transmission line can be modeled by the telegrapher's equation:

$$\begin{aligned}\frac{\partial V(x, t)}{\partial x} &= -L_l \frac{\partial I(x, t)}{\partial t} \\ \frac{\partial I(x, t)}{\partial x} &= -C_l \frac{\partial V(x, t)}{\partial t}\end{aligned}\tag{2.1}$$

where C_l and L_l are unit length capacitance and inductance. By combining these two equations into wave equations, one can easily shown that the phase velocity is $v_p = 1/\sqrt{L_l C_l}$. Moreover, the the waves can be decomposed into forward and backward propagation components:

$$\begin{aligned}V(x, t) &= V^+(t - \frac{x}{v_p}) + V^-(t + \frac{x}{v_p}) \\ I(x, t) &= \frac{1}{Z_0} \left[V^+(t - \frac{x}{v_p}) - V^-(t + \frac{x}{v_p}) \right]\end{aligned}\tag{2.2}$$

where $Z_0 = \sqrt{L_l/C_l}$ is the characteristic impedance of the line.

In RF applications, the characteristic impedance of a transmission line is often designed to be 50Ω . Such a design is to prevent impedance mismatch at connections, where microwaves will be partially reflected instead of smoothly transmitted. This is similar to EM wave reflection at dielectric interfaces with different dielectric constants.

A CPW consists of a central conductor (the signal line) with width w separated by two lateral ground planes with gaps s on a dielectric substrate [26]. For a nonmagnetic substrate, C_l and L_l are given by [26]:

$$\begin{aligned}L_l &= \frac{\mu_0 K(k'_0)}{4 K(k_0)} \\ C_l &= 4\epsilon_0\epsilon_{eff} \frac{K(k_0)}{K(k'_0)}\end{aligned}\tag{2.3}$$

where K denotes the complete elliptic integral of the first kind with the arguments $k_0 = w/(w + 2s)$ and $k'_0 = \sqrt{1 - k_0^2}$. When the substrate consists of a single layer of dielectric material with dielectric constant ϵ , the effective ϵ_{eff} can be roughly obtained by $\epsilon_{eff} \approx (\epsilon + 1)/2$, the average value of the substrate and air. In general,

the inductance of a superconducting CPW also includes kinetic inductance originating from the kinetic energy of Cooper pairs in superconductors due to low resistivity. Here we neglect the contribution from kinetic inductance for simplicity. Given the formula of L_l and C_l , we will provide our design parameters of CPW with characteristic impedance $Z_0 = \sqrt{L_l/C_l}$ close to 50Ω in the next Chapter.

2.2 CPW resonators and lumped element (LE) resonators

A CPW with open gaps at the two ends of the signal line will behave as a CPW resonator. Assume the open gaps with a distance l , the current in the device will have boundary conditions $I(0, t) = I(l, t) = 0$. Using the telegrapher's equation and separation of variables, we can write $I(x, t)$ and $V(x, t)$ as sum of multiple modes:

$$\begin{aligned} I(x, t) &= \sum_n i_n(t) \sin\left(\frac{n\pi}{l}x\right) \\ V(x, t) &= \sum_n v_n(t) \cos\left(\frac{n\pi}{l}x\right) \end{aligned} \tag{2.4}$$

where from the telegrapher equations, the dynamics of $i_n(t)$ and $v_n(t)$ must obey:

$$\begin{aligned} -\frac{n\pi}{l}v_n(t) &= -L_l \frac{di_n(t)}{dt} \\ \frac{n\pi}{l}i_n(t) &= -C_l \frac{dv_n(t)}{dt} \end{aligned} \tag{2.5}$$

We note that the dynamical equations resemble that of harmonic oscillators, implying resonant frequencies $\omega_n = n\pi/l\sqrt{L_l C_l}$. In a CPW, it is known that $1/\sqrt{L_l C_l} = 1/\sqrt{\mu_0 \epsilon_0 \epsilon_{eff}}$, which means that our derived resonant frequencies correspond to $f_n = nc/2l\sqrt{\epsilon_{eff}}$, where c is the speed of light [26]. Note that the spatial profile of $V(x, t)$ and $I(y, t)$ are mode-dependent. When coupling the CPW resonator to other quantum excitations, usually a mode of the resonator is targeted according to the frequency of the quantum excitations. Then, depending on whether capacitive (voltage) coupling

or inductive (current) coupling is utilized, the quantum system is put at the voltage or current antinode to enhance coupling, respectively.

A lumped element resonator is a realization of the LC circuit model. Compared to the CPW resonator, it does not have a distributive $I(x, t)$ and $V(x, t)$, rather it is modeled using $I(t)$ and $V(t)$:

$$\begin{aligned} V(t) &= L \frac{dI(t)}{dt} \\ I(t) &= -C \frac{dV(t)}{dt} \end{aligned} \tag{2.6}$$

Here we have chosen the convention such that the equations have similarity with those of CPW resonators. The resonant frequency can be easily obtained as $\omega_r^{LC} = 1/\sqrt{LC}$. In our thesis, a lumped element resonator is realized by connecting a large interdigitated capacitor in parallel with a small inductor. Note that, experimentally this resonator has more than one resonant modes. Therefore, the corresponding L and C is mode-dependent. It is known that the lowest frequency mode is a symmetric mode corresponds to a high current density passing through the central inductive wire. In this case, the capacitance of the interdigitated capacitor can be calculated analytically [33].

2.3 Quantization of superconducting resonators as LC circuits

In this section, we first treat the quantum mechanical model of an LC circuit for the lumped element resonator and then provide a field quantization description of the CPW resonator, where the distributive nature of modes is taken into account.

In a simple harmonic oscillator (SHO) with dynamical variables $x(t)$ and $p(t)$, a quantum mechanical model is developed by promoting the dynamical variables to quantum mechanical operators \hat{x} and \hat{p} with commutation relation $[\hat{x}, \hat{p}] = i\hbar$, and writing them in terms of creation and annihilation operators \hat{a}^\dagger and \hat{a} . Due to the similarity of equations of $I(t)$ and $V(t)$ in an LC circuit to the $x(t)$ and $p(t)$ equations

in a SHO, we expect that similar procedure applies. First of all, the Hamiltonian of the LC resonator is:

$$\hat{H}_r = \frac{1}{2}L\hat{I}^2 + \frac{1}{2}C\hat{V}^2$$

Then, we require that $[\hat{V}, \hat{I}] = i\hbar A$, where A is a constant to be determined, similar to $[\hat{x}, \hat{p}] = i\hbar$ in normal SHO. Next, we require that the time evolution of quantum expectation values match those of classical equations of motion. Such time evolutions are given by Ehrenfest's Theorem: $d\langle\hat{O}\rangle/dt = \langle[\hat{O}, \hat{H}]\rangle/i\hbar$ for general time independent operator \hat{O} . Our requirements become: $d\langle\hat{V}\rangle/dt = \langle[\hat{V}, \hat{H}_r]\rangle/i\hbar = -\langle\hat{I}\rangle/C$ and $d\langle\hat{I}\rangle/dt = \langle[\hat{I}, \hat{H}_r]\rangle/i\hbar = \langle\hat{V}\rangle/L$. These conditions fix $A = -1/LC$. Following the commutation relation and the requirement of equal energy distribution between inductive and capacitive parts, we write the operators \hat{I} and \hat{V} in terms of creation and annihilation operators:

$$\begin{aligned}\hat{V} &= i\omega_r\sqrt{\frac{\hbar Z_r}{2}}(\hat{a}_r^\dagger - \hat{a}_r) \\ \hat{I} &= \omega_r\sqrt{\frac{\hbar}{2Z_r}}(\hat{a}_r^\dagger + \hat{a}_r)\end{aligned}\tag{2.7}$$

where $Z_r = \sqrt{L/C}$ and $\omega_r = 1/\sqrt{LC}$ are the characteristic impedance and the resonant frequency of the LC resonator, respectively. With photon commutation relation $[\hat{a}_r^\dagger, \hat{a}_r] = 1$, one can check $[\hat{V}, \hat{I}] = -i\hbar/LC$ and $\langle L\hat{I}^2/2\rangle = \langle C\hat{V}^2/2\rangle$ are indeed satisfied. Accordingly, the Hamiltonian can be rewritten as in the form of SHO:

$$\hat{H}_r = \hbar\omega_r(\hat{a}_r^\dagger\hat{a}_r + \frac{1}{2})$$

Now we perform field quantization of CPW resonators. Following similar procedure, we promote dynamical variables $i_n(t)$ and $v_n(t)$ to quantum mechanical operators \hat{i}_n and \hat{v}_n , which form conjugate variables with commutation relation $[\hat{i}_n, \hat{v}_n] = i\hbar A_n$. To determine constant A_n , we first write the total Hamiltonian $\hat{H}_{CPW} = \int_0^l dx(\frac{1}{2}C_l\hat{V}^2 + \frac{1}{2}L_l\hat{I}^2) = \frac{l}{4}(C_l\sum_n\hat{v}_n^2 + L_l\sum_n\hat{i}_n^2)$. We require that the semiclassical equations derived from Ehrenfest Theorem reproduce the original dynamical equations: $d\langle\hat{v}_n\rangle/dt = \langle[\hat{v}_n, \hat{H}_{CPW}]\rangle/i\hbar = -lL_lA_n\langle\hat{i}_n\rangle/2 = -n\pi\langle\hat{i}_n\rangle/lC_l$ and $d\langle\hat{i}_n\rangle/dt =$

$\langle [\hat{i}, \hat{H}_{CPW}] \rangle / i\hbar = lC_l A_n \langle \hat{v}_n \rangle / 2 = n\pi \langle \hat{i}_n \rangle / lL_l$. This is achieved by $A_n = 2n\pi / C_l L_l l^2 = 2\omega_n / l\sqrt{L_l C_l}$. Following the commutation relation and the requirement of equal energy distribution between inductive and capacitive parts, we write the operators \hat{v}_n and \hat{i}_n in terms of creation and annihilation operators: $\hat{v}_n = i\sqrt{\hbar\omega_n / lC_l}(\hat{a}_n^\dagger - \hat{a}_n) = i\omega_n\sqrt{\hbar Z_0 / n\pi}(\hat{a}_n^\dagger - \hat{a}_n)$ and $\hat{i}_n = \sqrt{\hbar\omega_n / lL_l}(\hat{a}_n^\dagger + \hat{a}_n) = \omega_n\sqrt{\hbar / Z_0 n\pi}(\hat{a}_n^\dagger + \hat{a}_n)$, where $Z_0 = \sqrt{L_l / C_l}$ is the impedance of the CPW. It can be easily shown that $\hat{H}_{CPW} = \sum_n \hbar\omega_n(\hat{a}_n^\dagger \hat{a}_n + 1/2)$, a sum of multiple modes of harmonic oscillators. The original $I(x, t)$ and $V(x, t)$ now become field operators:

$$\begin{aligned}\hat{V}(x) &= \sum_n i\omega_n \sqrt{\frac{\hbar Z_0}{n\pi}} (\hat{a}_n^\dagger - \hat{a}_n) \cos\left(\frac{n\pi}{l}x\right) \\ \hat{I}(x) &= \sum_n \omega_n \sqrt{\frac{\hbar}{Z_0 n\pi}} (\hat{a}_n^\dagger + \hat{a}_n) \sin\left(\frac{n\pi}{l}x\right)\end{aligned}\tag{2.8}$$

When we apply this formulation to light-matter interaction, only a single resonator mode ($n = 1$ fundamental mode in our case) is interacting with the matter at a given frequency range. Note that the field operators description indicate position-dependent coupling strength between photons and the matter system. We can compare the form of field operators $\hat{V}(x)$ and $\hat{I}(x)$ with operators \hat{V} and \hat{I} in the LC circuit. Particularly, if capacitive (voltage) coupling is utilized and the matter is put at voltage antinode, the impedance "seen" by the matter is $Z_{r, capacitive}^{CPW} = 2Z_0 / n\pi$, where n is the CPW photon mode under consideration. On the other hand, if inductive (current) coupling is utilized and the matter is put at current antinode, the impedance "seen" by the matter is $Z_{r, inductive}^{CPW} = Z_0 n\pi / 2$. In this sense, a CPW resonator can be effectively viewed as a LC circuit when considering its effects on photon-matter coupled system.

2.4 Theoretical description of ferromagnetic resonance magnon modes

The study of magnetic resonance has a long history. In the case of uniform mode of ferromagnetic resonance (the Kittel mode), the dynamics of a magnetic moment $\hat{\mathbf{m}}$

is traditionally described by Landau-Lifshitz-Gilbert (LLG) equation:

$$\frac{d\hat{\mathbf{m}}}{dt} = -\mu_0\gamma\hat{\mathbf{m}} \times \mathbf{H}_{\text{eff}} + \alpha\hat{\mathbf{m}} \times \frac{d\hat{\mathbf{m}}}{dt}$$

where $\gamma/2\pi \approx 28\text{GHz/T}$ is the gyromagnetic ratio, α is the Gilbert damping coefficient, and \mathbf{H}_{eff} is the effective magnetic field exerted on $\hat{\mathbf{m}}$, which generally contains applied DC magnetic field and anisotropy field. \mathbf{H}_{eff} can be derived from free energy by the formula $\mathbf{H}_{\text{eff}} = -\frac{1}{\mu_0} \frac{\partial F}{\partial \mathbf{M}}$, where F is the free energy of the magnet and $\mathbf{M} = M_s \hat{\mathbf{m}}$, with M_s the saturation magnetization.

Here, we provide a derivation of the Kittel formula for resonant frequency of the Kittel mode, where shape anisotropy of the magnet plays an important role. The contribution of shape anisotropy to F can be written as $\frac{\mu_0}{2}(N_x M_x^2 + N_y M_y^2 + N_z M_z^2)$, where N_i are the demagnetization factors satisfying $\sum_i N_i = 1$. Assume the magnetic field $\mathbf{H}_{\text{ext}} = -H_0 \hat{\mathbf{z}}$ is applied, then the effective field is $\mathbf{H}_{\text{eff}} = (-N_x M_x, -N_y M_y, -H_0 - N_z M_z)$. Omitting the damping, the LLG equation writes:

$$\begin{aligned} \frac{dm_x}{dt} &= -\mu_0\gamma(-H_0 - N_z M_z)m_y + \mu_0\gamma(-N_y M_y)m_z \\ \frac{dm_y}{dt} &= -\mu_0\gamma(-N_x M_x)m_z + \mu_0\gamma(-H_0 - N_z M_z)m_x \\ \frac{dm_z}{dt} &= -\mu_0\gamma(-N_y M_y)m_x + \mu_0\gamma(-N_x M_x)m_y \end{aligned} \quad (2.9)$$

Here we focus on the small angle precession case, where $m_z \approx -1$. Then we get:

$$\begin{aligned} \frac{dm_x}{dt} &= -\mu_0\gamma(-H_0 + N_z M_s)m_y - \mu_0\gamma(-N_y M_s)m_y \\ \frac{dm_y}{dt} &= \mu_0\gamma(-N_x M_s)m_x + \mu_0\gamma(-H_0 + N_z M_s)m_x \end{aligned} \quad (2.10)$$

These equations indicate the circular (or elliptical if anisotropy is considered) precession of the magnetic moment around the applied field direction. We can therefore deduce $\frac{d^2 m_y}{dt^2} = -\omega^2 m_y$ and $\frac{d^2 m_x}{dt^2} = -\omega^2 m_x$ with resonant frequency

$$\omega = \mu_0\gamma\sqrt{(H_0 + (N_x - N_z)M_s)(H_0 + (N_y - N_z)M_s)}$$

which is the celebrated Kittel formula. The value of N_i 's can be calculated once shape of the magnet is given.

Now, we formulate the above equations in terms of quantum macrospin. First of all, the energy can be written as $\hat{H}_m = -\hat{\mathbf{M}} \cdot \mathbf{B}_0 + \frac{\mu_0}{2}(N_x \hat{M}_x^2 + N_y \hat{M}_y^2 + N_z \hat{M}_z^2)$. We now rewrite $\hat{\mathbf{M}} = -\frac{g_e \mu_B}{\hbar} \hat{\mathbf{S}} = -\gamma \hat{\mathbf{S}}$. Then, using Ehrenfest's Theorem and the commutation relation of the macrospin operators $[\hat{S}_i, \hat{S}_j] = i\hbar \epsilon_{ijk} \hat{S}_k$, where ϵ_{ijk} is the Levi-Civita symbol, we obtain:

$$\begin{aligned} \frac{d\langle \hat{S}_x \rangle}{dt} &= \gamma B_0 \langle \hat{S}_y \rangle + \frac{\mu_0}{2} \gamma^2 (N_y - N_z) \langle \hat{S}_y \hat{S}_z + \hat{S}_z \hat{S}_y \rangle \\ \frac{d\langle \hat{S}_y \rangle}{dt} &= -\gamma B_0 \langle \hat{S}_x \rangle + \frac{\mu_0}{2} \gamma^2 (N_z - N_x) \langle \hat{S}_x \hat{S}_z + \hat{S}_z \hat{S}_x \rangle \\ \frac{d\langle \hat{S}_z \rangle}{dt} &= \frac{\mu_0}{2} \gamma^2 (N_x - N_y) \langle \hat{S}_x \hat{S}_y + \hat{S}_y \hat{S}_x \rangle \end{aligned} \quad (2.11)$$

With the small precession approximation, $\gamma \langle S_z \rangle = M_s$. Then the equations become:

$$\begin{aligned} \frac{d\langle \hat{S}_x \rangle}{dt} &= \gamma B_0 \langle \hat{S}_y \rangle + \mu_0 \gamma (N_y - N_z) \langle \hat{S}_y \rangle M_s \\ \frac{d\langle \hat{S}_y \rangle}{dt} &= -\gamma B_0 \langle \hat{S}_x \rangle + \mu_0 \gamma (N_z - N_x) \langle \hat{S}_x \rangle M_s \end{aligned} \quad (2.12)$$

We see that the Kittel formula is recovered. We will use the quantum macrospin model for the derivation of magnon-photon coupling.

2.5 Magnon-photon coupled systems with LC circuits

We consider the quantum mechanical model of a quantum macrospin coupled to an LC resonator through oscillating magnetic field generated by the inductor. The macrospin model is justified as we observe the uniform ferromagnetic resonance mode, Kittel mode, in the experiment [62, 23]. The LC circuit model has been widely adopted to describe the photon modes of superconducting resonators in the context of Circuit QED. The Hamiltonian is composed of three parts: LC resonator $\hat{H}_r =$

$L\hat{I}^2/2 + C\hat{V}^2/2$, magnon $\hat{H}_m = g_e\mu_B/\hbar\hat{\mathbf{S}} \cdot \mathbf{B}_{\text{eff}}$, and interaction $\hat{H}_{int} = g_e\mu_B/\hbar\hat{\mathbf{S}} \cdot \hat{\mathbf{B}}_{\text{rf}} = g_e\mu_B/\hbar\hat{\mathbf{S}} \cdot \mathbf{b}_{\text{rf}}\hat{I}$, where \mathbf{b}_{rf} is the magnetic field experienced by the macrospin per unit inductor current. The effective field of the magnon \mathbf{B}_{eff} generally contains contributions from external field \mathbf{B}_{ext} as well as magnetic anisotropy, which we neglect for simplicity. The macrospin operators satisfy the commutation relation $[\hat{S}_i, \hat{S}_j] = i\hbar\epsilon_{ijk}\hat{S}_k$, where ϵ_{ijk} is the Levi-Civita symbol. To match our experimental setup, we adopt $\mathbf{B}_{\text{ext}} = -B_0\hat{\mathbf{z}}$ and $\mathbf{b}_{\text{rf}} = b_{\text{rf}}\hat{\mathbf{x}}$. The total Hamiltonian can thus be written as :

$$\begin{aligned}\hat{H} &= \hat{H}_r + \hat{H}_m + \hat{H}_{int} \\ &= \frac{1}{2}L\hat{I}^2 + \frac{1}{2}C\hat{V}^2 + \frac{g_e\mu_B}{\hbar}\hat{\mathbf{S}} \cdot \mathbf{B}_{\text{ext}} + \frac{g_e\mu_B}{\hbar}\hat{\mathbf{S}} \cdot \hat{\mathbf{B}}_{\text{rf}} \\ &= \frac{1}{2}L\hat{I}^2 + \frac{1}{2}C\hat{V}^2 - \frac{g_e\mu_B}{\hbar}B_0\hat{S}_z + \frac{g_e\mu_B b_{\text{rf}}}{\hbar}\hat{S}_x\hat{I}\end{aligned}\quad (2.13)$$

Note that without the interaction Hamiltonian \hat{H}_{int} , the ground state of the macrospin is with $\langle\hat{\mathbf{S}}\rangle = \hbar S\hat{\mathbf{z}}$ where the macrospin with total spin S is aligned in positive z -direction by the external field. To proceed, we express the macrospin operator $\hat{\mathbf{S}} = \frac{1}{2}(\hat{S}_+ + \hat{S}_-)\hat{\mathbf{x}} + \frac{1}{2i}(\hat{S}_+ - \hat{S}_-)\hat{\mathbf{y}} + \hat{S}_z\hat{\mathbf{z}}$, with \hat{S}_+ (\hat{S}_-) raising (lowering) the z -component of the macrospin. We also express operators \hat{V} and \hat{I} in terms of creation (annihilation) operators of photon modes in the resonator \hat{a}_r^\dagger (\hat{a}_r): $\hat{V} = i\omega_r\sqrt{\hbar Z_r/2}(\hat{a}_r^\dagger - \hat{a}_r)$ and $\hat{I} = \omega_r\sqrt{\hbar/2Z_r}(\hat{a}_r^\dagger + \hat{a}_r)$, where $Z_r = \sqrt{L/C}$ and $\omega_r = 1/\sqrt{LC}$ are the characteristic impedance and the resonant frequency of the LC resonator, respectively. Note that in this LC circuit quantization convention, the semiclassical equations of motion without the macrospin are $d\langle\hat{V}\rangle/dt = \langle[\hat{V}, \hat{H}_r]\rangle/i\hbar = -\langle\hat{I}\rangle/C$ and $d\langle\hat{I}\rangle/dt = \langle[\hat{I}, \hat{H}_r]\rangle/i\hbar = \langle\hat{V}\rangle/L$ obtained by Ehrenfest Theorem ($d\langle\hat{O}\rangle/dt = \langle[\hat{O}, \hat{H}]\rangle/i\hbar$ for general time independent operator \hat{O}), which resembles dynamics of a classical LC circuit. Moreover, the equations of motion of the macrospin without the LC resonator can be obtained as $d\langle\hat{S}_x\rangle/dt = \langle[\hat{S}_x, \hat{H}_m]\rangle/i\hbar = g_e\mu_B B_0\langle\hat{S}_y\rangle/\hbar$ and $d\langle\hat{S}_y\rangle/dt = \langle[\hat{S}_y, \hat{H}_m]\rangle/i\hbar = -g_e\mu_B B_0\langle\hat{S}_x\rangle/\hbar$, which represents circular precession of the magnon mode. With the above expressions of operators and adopting rotating

wave approximation, the Hamiltonian can now be written as:

$$\begin{aligned}\hat{H} &= \hbar\omega_r(\hat{a}_r^\dagger\hat{a}_r + \frac{1}{2}) - \frac{g_e\mu_B}{\hbar}B_0\hat{S}_z + \frac{g_e\mu_B b_{\text{rf}}\omega_r}{\hbar}\sqrt{\frac{\hbar}{8Z_r}}(\hat{S}_+\hat{a}_r^\dagger + \hat{S}_-\hat{a}_r) \\ &= \hbar\omega_r(\hat{a}_r^\dagger\hat{a}_r + \frac{1}{2}) - \omega_m(B_0)\hat{S}_z + g_s(\hat{S}_+\hat{a}_r^\dagger + \hat{S}_-\hat{a}_r)\end{aligned}\quad (2.14)$$

where $\omega_m(B_0) = g_e\mu_B B_0/\hbar$ and $g_s = g_e\mu_B b_{\text{rf}}\omega_r/\sqrt{8\hbar Z_r}$ are the magnon frequency (a function of applied field B_0) and single spin-photon coupling strength which will become clear shortly, respectively. We can now compute the time evolution of expectation values of resonator and macrospin operators using Ehrenfest Theorem:

$$\begin{aligned}\frac{d\langle\hat{a}_r\rangle}{dt} &= -i\omega_r\langle\hat{a}_r\rangle - i\frac{g_s}{\hbar}\langle\hat{S}_+\rangle \\ \frac{d\langle\hat{S}_+\rangle}{dt} &= -i\omega_m(B_0)\langle\hat{S}_+\rangle - i2g_s\langle\hat{a}_r\hat{S}_z\rangle \\ \frac{d\langle\hat{a}_r^\dagger\rangle}{dt} &= i\omega_r\langle\hat{a}_r^\dagger\rangle + i\frac{g_s}{\hbar}\langle\hat{S}_-\rangle \\ \frac{d\langle\hat{S}_-\rangle}{dt} &= i\omega_m(B_0)\langle\hat{S}_-\rangle + i2g_s\langle\hat{a}_r^\dagger\hat{S}_z\rangle\end{aligned}\quad (2.15)$$

Here we assume that the amplitude of magnetic oscillation is small such that the state is approximately an eigenstate of \hat{S}_z with eigenvalue $\hbar S = \frac{\hbar N}{2}$, where N is the total number of spins mentioned in the main text. In this assumption, the upper two equations are decoupled from the lower two equations. Moreover, the algebraic structure is similar to coupled harmonic oscillators. We assume harmonic time dependence $\langle\hat{a}_r\rangle = a_0 e^{i\omega t}$ and $\langle\hat{S}_+\rangle = S_0 e^{i\omega t}$. The upper two equations indicate the eigenvalue problem:

$$\begin{pmatrix} \omega - \omega_r & g_s/\hbar \\ Ng_s\hbar & \omega - \omega_m(B_0) \end{pmatrix} \begin{pmatrix} a_0 \\ S_0 \end{pmatrix} = 0\quad (2.16)$$

The eigenvalue equation gives two resonant frequencies: $\omega_{\pm} = \omega_r + \frac{\Delta}{2} \pm \sqrt{\Delta^2 + 4g^2}$, where $\Delta = \omega_m(B_0) - \omega_r$ is the detuning and $g = g_s\sqrt{N}$ is the total magnon-photon coupling strength. The coupled modes dispersion describes the character-

istic anticrossing observed in experiment. Here we note the scaling of coupling strength with number of spins $g = g_s\sqrt{N}$, with the single spin coupling strength $g_s = g_e\mu_B b_{rf}\omega_r/\sqrt{8\hbar Z_r}$ [20] derived in a quantum mechanical manner. The semiclassical model expresses classical physical quantities (such as $I(t)$ and $S_x(t)$) in terms of quantum expectation values of operators (such as $\langle \hat{I} \rangle$ and $\langle \hat{S}_x \rangle$), whose time evolutions are related to those of $\langle \hat{a}_r \rangle$ and $\langle \hat{S}_+ \rangle$, together with $\langle \hat{a}_r^\dagger \rangle = \langle \hat{a}_r \rangle^*$ and $\langle \hat{S}_- \rangle = \langle \hat{S}_+ \rangle^*$. The constants $a_{0\pm}$ and $S_{0\pm}$ can be determined by initial conditions of the problem in consideration. This can be adopted to describe "Rabi-like" oscillations in magnon-photon coupled systems in classical region [76].

We can also rewrite the Hamiltonian using Holstein-Primakoff transformation which expresses the macrospin operators as magnon excitation boson operators \hat{a}_m^\dagger and \hat{a}_m :

$$\begin{aligned}\hat{S}_- &= \hbar \hat{a}_m^\dagger \sqrt{2S - \hat{a}_m^\dagger \hat{a}_m} \\ \hat{S}_+ &= \hbar \sqrt{2S - \hat{a}_m^\dagger \hat{a}_m} \hat{a}_m \\ \hat{S}_z &= \hbar S - \hbar \hat{a}_m^\dagger \hat{a}_m\end{aligned}\tag{2.17}$$

Again, we assume the magnon excitation is small ($\langle \hat{a}_m^\dagger \hat{a}_m \rangle / S \ll 1$) and neglect the term $\hat{a}_m^\dagger \hat{a}_m$ in the transformation for \hat{S}_- and \hat{S}_+ . The total spin is $S = N/2$. We drop the constant energy terms and get the Hamiltonian:

$$H = \hbar\omega_r \hat{a}_r^\dagger \hat{a}_r + \hbar\omega_m(B_0) \hat{a}_m^\dagger \hat{a}_m + \hbar g_s \sqrt{N} (\hat{a}_m \hat{a}_r^\dagger + \hat{a}_m^\dagger \hat{a}_r)\tag{2.18}$$

The time evolution of the operators can be computed:

$$\begin{aligned}\frac{d\langle \hat{a}_r \rangle}{dt} &= -i\omega_r \langle \hat{a}_r \rangle - ig_s \sqrt{N} \langle \hat{a}_m \rangle \\ \frac{d\langle \hat{a}_m \rangle}{dt} &= -i\omega_m(B_0) \langle \hat{a}_m \rangle - ig_s \sqrt{N} \langle \hat{a}_r \rangle \\ \frac{d\langle \hat{a}_r^\dagger \rangle}{dt} &= i\omega_r \langle \hat{a}_r^\dagger \rangle + ig_s \sqrt{N} \langle \hat{a}_m^\dagger \rangle \\ \frac{d\langle \hat{a}_m^\dagger \rangle}{dt} &= i\omega_m(B_0) \langle \hat{a}_m^\dagger \rangle + ig_s \sqrt{N} \langle \hat{a}_r^\dagger \rangle\end{aligned}\tag{2.19}$$

The upper two equations are already decoupled from the lower two, due to the assumption of small magnon excitation. We assume harmonic time dependence $\langle \hat{a}_r \rangle = a_{r0} e^{i\omega t}$ and $\langle \hat{a}_m \rangle = a_{m0} e^{i\omega t}$. We get eigenvalue equation:

$$\begin{pmatrix} \omega - \omega_r & g_s \sqrt{N} \\ g_s \sqrt{N} & \omega - \omega_m(B_0) \end{pmatrix} \begin{pmatrix} a_{r0} \\ a_{m0} \end{pmatrix} = 0 \quad (2.20)$$

We again obtain $\omega_{\pm} = \omega_r + \frac{\Delta}{2} \pm \sqrt{\Delta^2 + 4g^2}$, where $g = g_s \sqrt{N}$ is the total magnon-photon coupling strength.

From the above derivation, $g = g_s \sqrt{N}$ is the total magnon-photon coupling strength, with $g_s = g_e \mu_B b_{\text{rf}} \omega_r / \sqrt{8\hbar Z_r}$ [20]. Therefore, in order to achieve scalable strong magnon-photon coupling with reduced N , it is important to increase the value of g_s . For fixed resonant frequency of the resonator, two strategies can be employed to achieve this: (i) increasing b_{rf} by adjusting geometry of the inductive wire, or by placing the magnet close to the location with maximum magnetic field in the resonator; (ii) reducing Z_r by utilizing low-impedance resonators with small L and large C . In this thesis, by adopting the first strategy in a superconducting CPW resonator, we first realize a relatively high $g_s^{\text{CPW}}/2\pi = 18$ Hz by depositing the Permalloy stripe directly on top of the signal line with a thin insulating insertion, where strong coupling is realized with as few as 10^{13} spins. Furthermore, by combining both strategies, we show that very high coupling $g_s^{\text{LE}}/2\pi = 263$ Hz can be achieved in a lumped element LC resonator, which allows another two orders of magnitude reduction in spin number N to achieve similar coupling strength. The experimental data will be presented in Chapter 4.

Chapter 3

Experimental Setups

In this Chapter, we present our experimental setups for realizing magnon-photon coupled systems using lithographically defined superconducting resonators. We will first discuss the choice of materials and device structure, and present the device fabrication procedure. Finally, we discuss our measurement setup including microwave measurement system incorporated with cryogenics and printed circuit board (PCB).

3.1 Material and device design

To realize magnon-photon coupling using superconducting resonators, our device must consist of a substrate, a superconducting thin-film resonator, and patterned magnetic material in proximity to the resonator. The choice of materials and the device structure should be taken into account at the same time for the successful demonstration of the coupled system.

First of all, the choice of magnetic material determines our device structure. In previous reported literatures, magnon-photon coupled systems are all realized using yttrium iron garnet (YIG), to our best knowledge. YIG is an insulating ferrimagnet with very low damping coefficient ($\alpha < 0.001$) which suits for reaching strong coupling. However, so far the growth of high quality YIG thin film highly relies on the substrate. The most common choice for YIG growth is Gadolinium Gallium Garnet (GGG) substrate due to their matched lattice constant [17]. Therefore, it is not yet

possible to directly grow high quality YIG on top of the superconducting resonator. So a different approach, a flip-chip design was utilized with the detection of magnons from YIG in a previous literature, which results in air-gaps and reduced coupling strength. Moreover, the system would not be an on-chip and scalable design.

Here, we utilize the Permalloy (Permalloy=Py=NiFe) instead, which is a ferromagnetic metal with higher damping coefficient ($\alpha > 0.004$). The growth of Py is not limited to the choice of substrates, and can be grown by magnetron sputtering in room temperature. Although there is no successful demonstration of magnon-photon coupled system using ferromagnetic metal in current literatures, we expect the underlying physics to be similar. Moreover, we note that various spintronic devices which utilize metallic magnetic materials, such as magnetic tunnel junctions, have been developed independently. Therefore, a successful demonstration of the coupled system using metallic ferromagnet will open up the possibility to investigate magnon-photon coupling in a wide range of spintronic devices. Moreover, the whole system can be fabricated on a conventional Si-substrate using lithography process, which shows high potential for integrated hybrid quantum systems applications.

Besides the magnetic material, we choose Nb as the superconducting material with commonly reported critical temperature $T_c \approx 9$ K, which is well-below the temperature of our cryogenic setup (1.5 K). Moreover, Nb is a type-II superconductor, which possesses higher critical magnetic field compared to Al (a type-I superconductor). In our experiment, we have successfully demonstrated high quality factor Nb resonator with in-plane applied field greater than 6000 Oe. It should be noted that the direct growth of Py on top of the Nb will destroy the resonance, due to the conflict between ferromagnetic exchange interaction and singlet Cooper pairing. Therefore, we choose to deposit thin (~ 5 nm) MgO, a thin and high quality insulating layer, between Nb and Py. Moreover, it is known that Py is subject to oxidation when exposed to air. Therefore, a capping layer (Ta or Pt) is grown on top of the Py for protection.

Finally, we use high resistivity ($\rho > 10000 \Omega\text{cm}$) undoped Si-substrate. The high resistivity substrate is crucial for realizing high quality factor superconducting resonators.

3.2 Device fabrication

Our fabrication processes mainly consist of magnetron sputtering for material growth, photolithography for photoresist mask, Ar ion milling for resonator etching, and liftoff for Py bar formation. We describe the fabrication steps in detail as follows:

1. DC magnetron sputtering of 50 nm Nb on 500 μm thick Si substrate, with chamber pressure $< 2 \times 10^{-8}$ Torr for superconducting Nb.
2. Coating of the SPR-700 photoresist with a speed of 3000 rpm for 30 s, followed by a baking at 110°C for 3 minutes.
3. Defining the pattern for superconducting resonators and cross alignment markers. MLA-150 laser write with 375 nm light with dose 250 mJ/cm² used to expose the resist for patterning.
4. Develop of the photoresist in CD-26 developer for 55 s.
5. Ar ion milling for 20 minutes to etch away the Nb.
6. Soaking the etched sample in Microstrip with temperature 110°C for one hour to remove the resist.
7. Repeat steps 2-4 for the pattern for Py bar pattern. However, alignment is used to locate the Py bars accurately on top of the resonators.
8. Oxygen plasma with power 110 W for 1 minute to clean the organic residue before depositing Py bar.
9. Cover the device edge with Kapton tape before material growth for better liftoff results.
10. RF magnetron sputtering for growing 5 nm MgO and then DC magnetron sputtering for growing Py, followed by Ta or Pt capping layer.
11. Soaking of the sample in acetone for lift-off. The magnetic bar is formed.
12. Coating the SPR-700 photoresist on the chip. Use diesaw machine to cut the chip into devices with dimension smaller than 5mm by 5mm. Soak into acetone to remove the resist.

3.3 Measurement setup and procedure

Here, we first introduce our device mounting scheme onto the printed circuit board (PCB) shown in Fig. 3-1a. The PCB itself is a CPW on one side and a ground at the backside, and the dielectric material is FR-4. We mount the device on the PCB with cement glue (nonconducting) carefully with the long-axis of magnetic bar perpendicular to the signal line of the PCB. The device is wire-bonded with several Al wires to ensure good grounding of the device and microwave transmission through

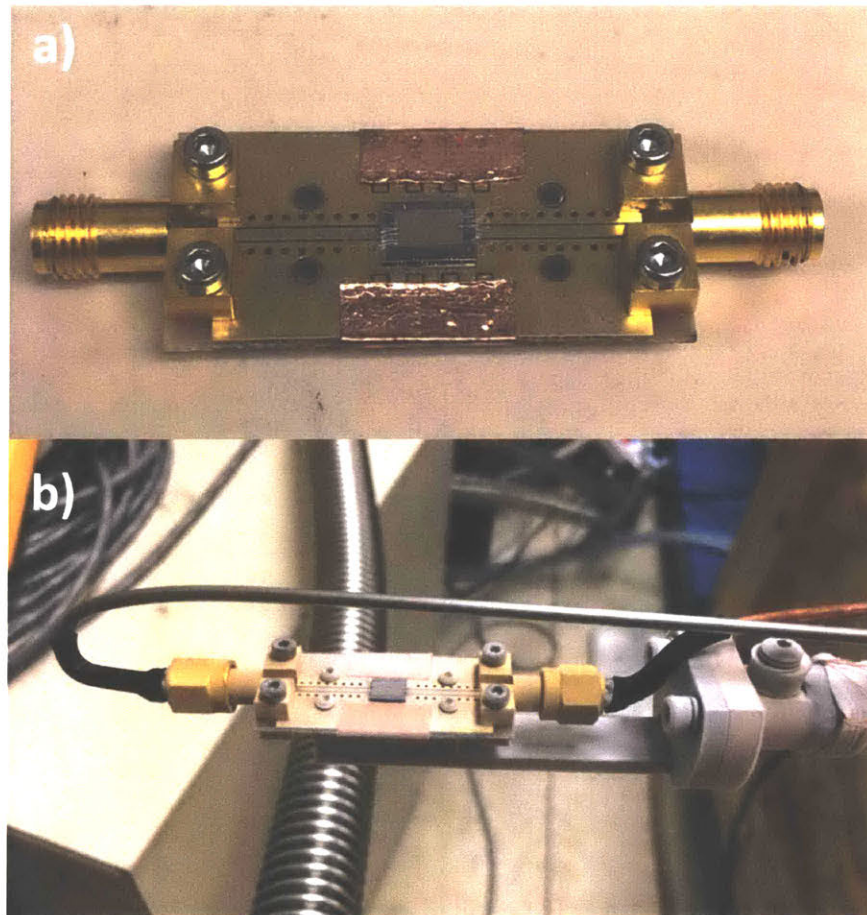


Figure 3-1: a) A PCB with a CPW resonator device. The signal line and the ground of the resonator device are wired-bonded to the signal line and the ground of the PCB, respectively. Note that several wires are bonded to ensure good microwave transmission. b) The PCB is mounted to the sample holder with screws to ensure thermal contact. The SMA connectors on the PCB are connected to RF coaxial cables.

the signal line. Besides SMA connectors for RF coaxial cable connection, the PCB also consists of eight DC pads. In the photo, they are grounded using Cu conducting tapes to minimize influence to the microwave transmission measurement. After wire-bonding, the PCB is mounted on the sample holder with screws and connected with RF coaxial cables, as shown in Fig. 3-1b.

The sample holder is attached to the bottom of the sample rod, which is inserted in a Janis 1.5 K cryostat with magnet setup, shown in Fig. 3-2. The rod orientation is carefully aligned so that the device plane is parallel with the external magnetic

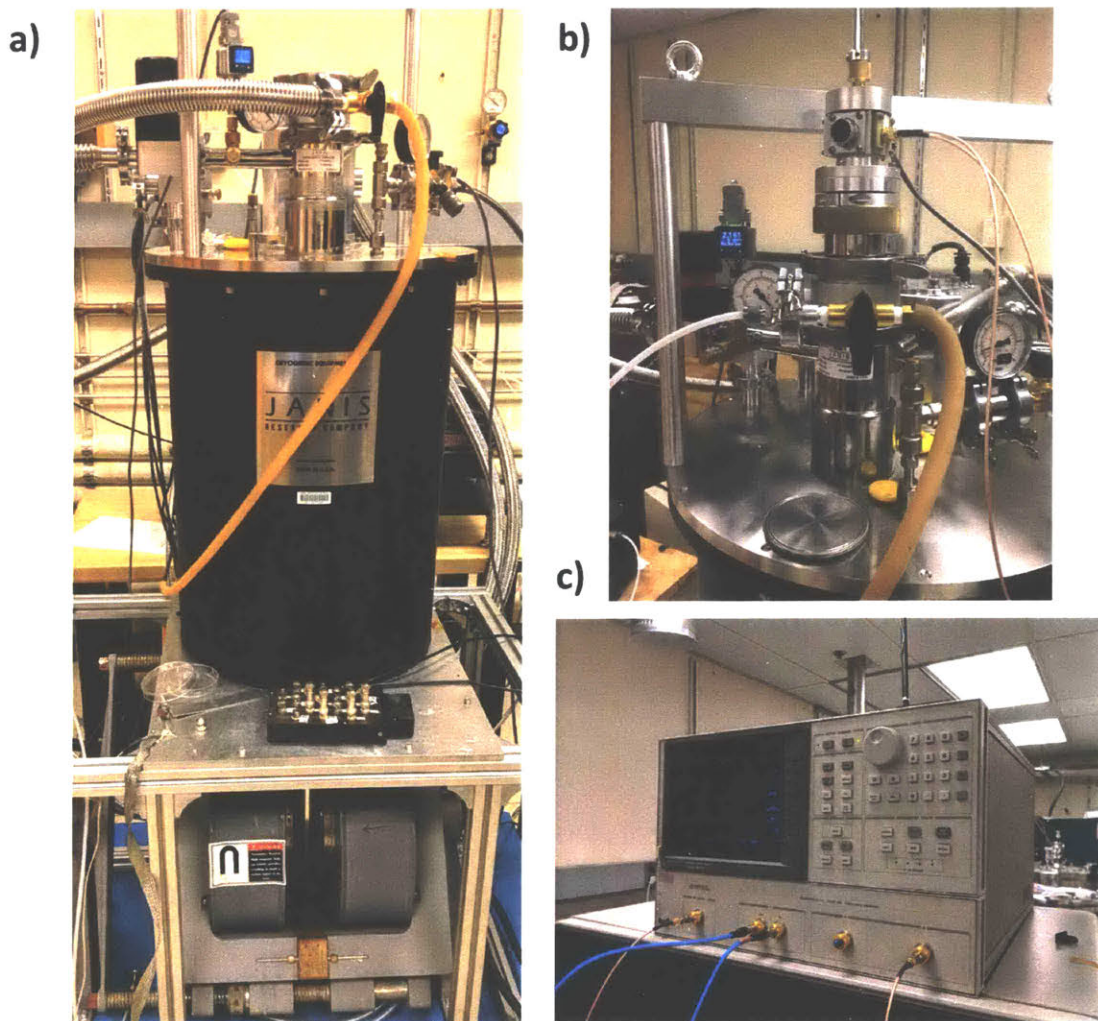


Figure 3-2: **a)** The Janis 1.5 K cryostat with a magnet setup at the bottom. **b)** Cryostat with the sample rod inserted. The sample rod consists of feedthrough for external RF cable connection. **c)** The Vector Network Analyzer (VNA) for microwave transmission measurement.

field direction. The alignment is made with the assist of markers, which were drawn according to previous measurements whose orientation maximized the quality factor of a superconducting resonator under applied magnetic field. Finally, the feedthrough on the sample rod allows RF cables connection to a Vector Network Analyzer (VNA) for microwave transmission measurement.

Chapter 4

Experiments of Magnon-Photon Coupled Systems using Superconducting Resonators

In this Chapter, we present our experimental results of magnon-photon coupled systems using lithographically defined superconducting resonators with two designs, the CPW resonators and the low-impedance lumped element (LE) resonators.

4.1 Simulation and characterization of CPW resonators

An image of the Nb CPW resonators with Py deposited on top is shown in Fig. 4-1. To enhance the microwave magnetic field generated by unit inductor current b_{rf} , we minimize the width of the CPW resonator signal line in Fig. 4-1 to be $w^{\text{CPW}} = 20 \mu\text{m}$. The $l = 12 \text{ mm}$ long resonator is then capacitively coupled to the external circuit through two gaps at the ends of signal line, leading to a fundamental resonant frequency $\omega_r/2\pi = c/2l\sqrt{\epsilon_{eff}} \approx 4.96 \text{ GHz}$, where c is the speed of light and $\epsilon_{eff} = 6.35$ represents the average dielectric constant of vacuum and Si substrate [26]. The fundamental mode has a current distribution which reaches maximum at the center of the signal line, where we deposit a MgO(5nm)/Py(50nm)/Pt(10nm) stripe by magnetron sputtering followed by liftoff. The thin insulating MgO layer protects

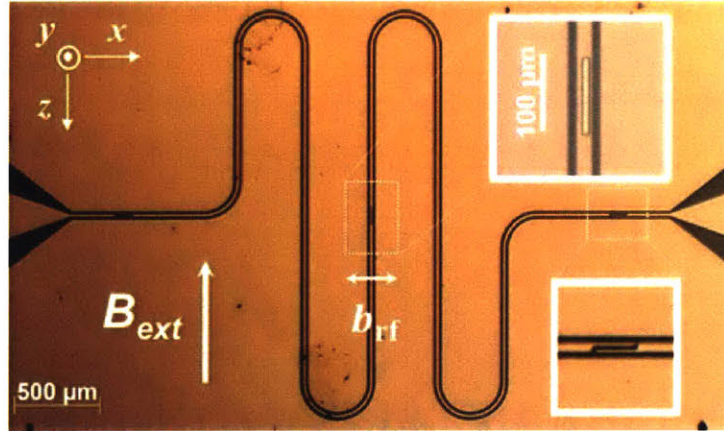


Figure 4-1: Photo of a CPW resonator device with $100\mu\text{m}\times 8\mu\text{m}\times 50\text{nm}$ MgO/Py/Pt stripe deposited at the center of the signal line. The distance $l = 12$ mm between the two open gaps at the ends of CPW defines the fundamental resonant frequency to be 4.96 GHz.

superconducting Nb from ferromagnetic exchange coupling, while bringing Py close to the surface of Nb for large RF magnetic field.

We use Sonnet microwave simulation package to simulate the transmission coefficient S_{21} of our CPW resonator design. From the simulation in Fig. 4-2a, two

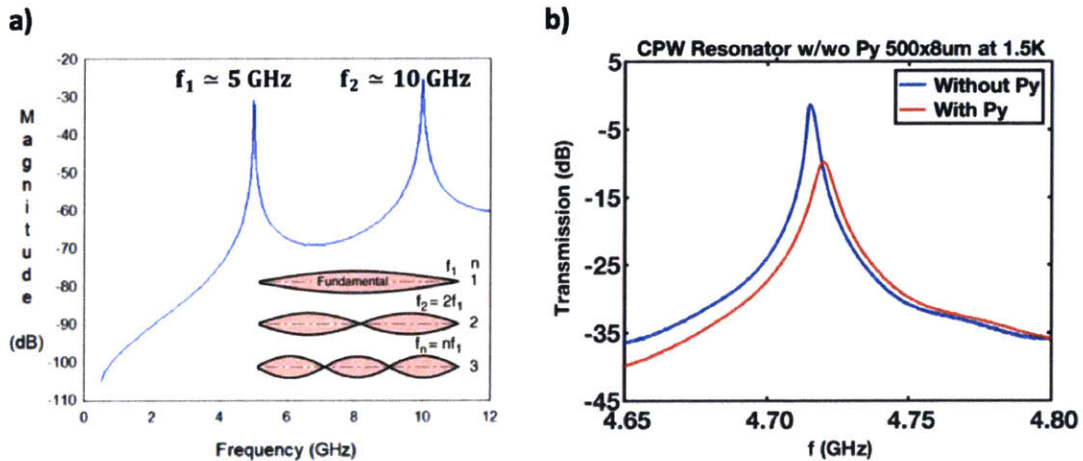


Figure 4-2: a) Microwave transmission simulated using Sonnet. Lossless conductor with zero thickness is assumed for the superconducting Nb structure. b) Microwave transmissions at 1.5 K with zero applied field before and after Py is deposited, exhibiting resonance signals with quality factors 1570 and 760, respectively. With Py, the resonator mode is blue detuned due to residual coupling to the magnon mode.

transmission peaks with frequencies around 5 GHz and 10 GHz are clearly seen, indicating first and second harmonic resonant modes. Experimentally, we mount the device in a cryostat with a base temperature of 1.5 K and studied the transmission of microwave signal with a Vector Network Analyzer. The transmission of the resonator before and after the deposition of Py stripe at zero field is shown in Fig. 4-2b, where the quality factor can be determined to be $Q = 1570$ and 760 , separately.

4.2 Magnon-photon coupled systems using CPW resonators

To measure the magnon-photon coupling, we have to tune the frequency of magnetic resonance. An in-plane magnetic field \mathbf{B}_{ext} is applied along the long axis direction of Py stripe. As the RF magnetic field produced by the signal line is perpendicular to the external field direction, the ferromagnetic resonance (FMR) mode can be excited, thereby inducing a microwave photon-magnon coupling. Fig. 4-3a shows the transmission of a sample with $500\mu\text{m} \times 8\mu\text{m}$ lateral dimensions as a function of frequency

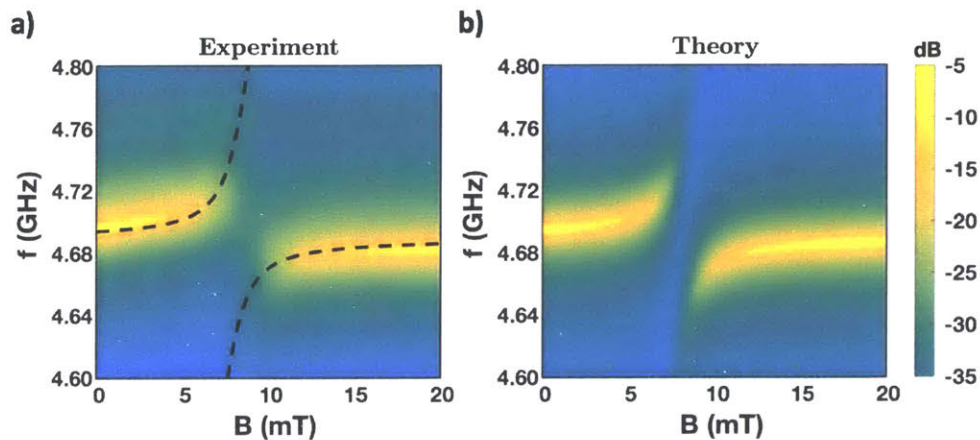


Figure 4-3: a) Microwave transmission as a function of frequency and in-plane magnetic field at 1.5 K for a sample with $500\mu\text{m} \times 8\mu\text{m} \times 50\text{nm}$ Py showing characteristic anti-crossing of magnon-photon coupling. b) Theoretical microwave transmission spectrum calculated using input-output theory with parameters obtained from the experiment.

and applied magnetic field. The distinct anti-crossing feature at $B_0 = 8$ mT is a result of microwave photon-magnon coupling where interaction between the two modes lift the degeneracy in resonance frequencies. The resonant modes evolution can be fitted by Eq. , with $\omega_m(B_0) = \gamma\sqrt{[B_0 + (N_y - N_z)\mu_0 M_s][B_0 + (N_x - N_z)\mu_0 M_s]}$ given by Kittel formula, where $\gamma/2\pi \approx 28$ GHz/T is the gyromagnetic ratio. In $\omega_m(B_0)$, the demagnetization factors N_i are taken into account, which can be analytically calculated with the dimension of the Py stripe [?]. Through the fitting, we extract the coupling strength $g/2\pi = 64$ MHz, the saturation magnetization $\mu_0 M_s = 1.2$ T of the Py stripe, and the resonator frequency $\omega_r^{\text{CPW}}/2\pi = 4.690$ GHz. Furthermore, we obtain the decay rates of the resonator mode $\kappa_r/2\pi = 1.5$ MHz and magnon mode $\kappa_m/2\pi = 122$ MHz by a transmission measurement of bare resonators and an independent FMR measurement of Py(50nm)/Pt(10nm) bilayer, separately.

To validate the coupling strength and decay rates, we adopt the input-output theory which gives microwave transmission coefficient as a function of frequency and magnetic field in our system [?, 32]:

$$S_{21}(\omega, B_0) = \frac{\kappa_{r,i}}{i(\omega - \omega_r) - \kappa_r + \frac{g^2}{i(\omega - \omega_m(B_0)) - \kappa_m/2}} \quad (4.1)$$

where $\kappa_{r,i}$ describes the external coupling rate to the cavity and only results in a constant offset in unit of dB. With the parameters measured in our experiment, we plot the theoretical transmission spectrum in Fig. 4-3b, which attains reasonable agreement with the experiment results, with the minimum transmission signal of the latter limited by the background level.

Using M_s and the magnetic volume of the Py stripe, we estimate the number of spins involved in the coupling to be $N = 2.1 \times 10^{13}$. To investigate the scaling of coupling strength with spin number, we fabricate devices with different sizes of Py stripes. The results are summarized in Table. 4.1. In the device with 2000 μm long Py, coupling strength $g/2\pi = 171$ MHz is obtained which is larger than κ_r and κ_m , and therefore falls into the strong coupling region. The corresponding cooperativity $g^2/\kappa_r\kappa_m = 160$ is very high for this small magnetic volume.

Py size	f_{res} (GHz)	$\mu_0 M_s$ (T)	$g/2\pi$ (MHz)
$2mm \times 8\mu m$	4.699	1.25	171.9
$500\mu m \times 8\mu m$	4.689	1.20	64.3
$100\mu m \times 8\mu m$	4.694	1.23	35.3
$50\mu m \times 8\mu m$	4.689	1.25	21.0
$50\mu m \times 4\mu m$	4.694	1.13	8.2

Table 4.1: Table for different CPW resonators with Py 50 nm thick deposited.

4.3 Simulation and characterization of LE resonators

Here, we adopt the strategy of impedance reduction to further enhance the coupling strength. Low-impedance lumped element (LE) LC resonator has been recently employed for paramagnetic electron spin resonance experiments [20, 9, 10], but the potential for reaching strong magnon-photon coupling remains largely unexplored. As is shown in Fig. 4-4, the resonator consists of large inter-digitated capacitors in parallel with a small inductor, and is capacitively side-coupled to the signal line of a CPW. The measured transmission coefficient of this resonator is shown in Fig. 4-5, where a minimum transmission shows up under the resonant condition due to its absorptive nature, in contrast to transmission peaks observed in the CPW resonator. Two resonant modes are observed in the transmission of the bare resonator, with reso-

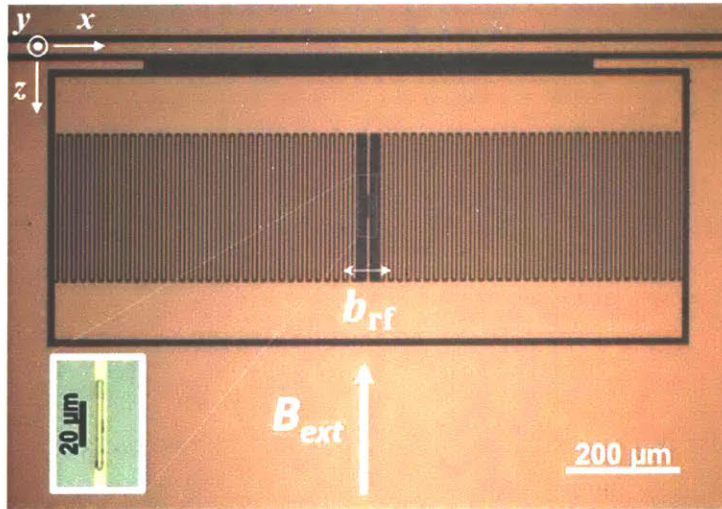


Figure 4-4: Image of a low-impedance lumped element resonator device with $40\mu m \times 2\mu m \times 10nm$ MgO/Py/Ta stripe deposited at the center of the $4\mu m$ wide inductive wire.

nant frequencies located at 5.42 and 9.19 GHz, separately. In order to understand the properties of the two modes, we carried out electromagnetic wave simulations (Sonnet) and found that the lower frequency mode corresponds to the case with a high current density passing through the central inductive wire (see simulation results in Fig. 4-5). We estimate the capacitance C of this mode analytically [33] to be 1.91 pF and obtain the corresponding inductance $L = 0.45$ nH using the measured ω_r . The characteristic impedance of this LC circuit is calculated to be $Z_r^{\text{LE}} = \sqrt{L/C} \approx 15.3 \Omega$, much smaller than the value of CPW resonators. Moreover, the inductor width w^{LE} is designed to be only $4 \mu\text{m}$ to further increase magnetic field intensity.

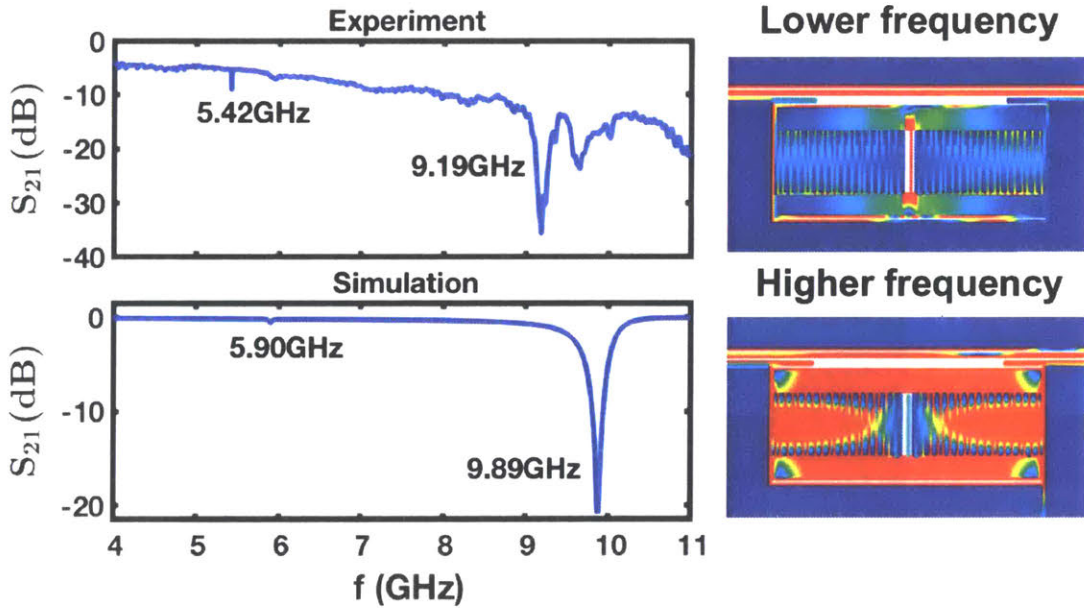


Figure 4-5: Left: Microwave transmission of the low-impedance resonator obtained from experiment and simulation. Two modes are observed as transmission minima due to photon absorption from the signal line. Right: Simulation of current density distribution of the resonant modes, respectively. Red and blue color indicates regions with strong and weak current densities, respectively. The first harmonic mode exhibits large current density at the central inductive wire which enhances coupling.

4.4 Magnon-photon coupled systems using LE resonators

Fig. 4-6 shows the transmission of a resonator that is coupled with a $40\mu\text{m} \times 2\mu\text{m} \times 10\text{nm}$ Py wire, as a function of frequency and applied magnetic field. Fitting the resonant frequencies evolution using Eq. , we extract the coupling strength $g/2\pi = 74.5$ MHz, the saturation magnetization $\mu_0 M_s = 1.1$ T, and the resonator frequency $\omega_r^{\text{LE}}/2\pi = 5.253$ GHz. The relatively smaller M_s value compared with that of the previous CPW resonator sample comes from the thinner Py film thickness (10 nm vs 50 nm) and potential magnetically dead interfacial layer [53]. With decay rates of the resonator mode $\kappa_r/2\pi = 1.05$ MHz and magnon mode $\kappa_m/2\pi = 122$ MHz, we calculate the cooperativity $g^2/\kappa_r\kappa_m = 43.3$, which is fairly large considering the very small number of spins ($N = 7.3 \times 10^{10}$).

To investigate the scaling of coupling strength with magnetic volume, we fabricate

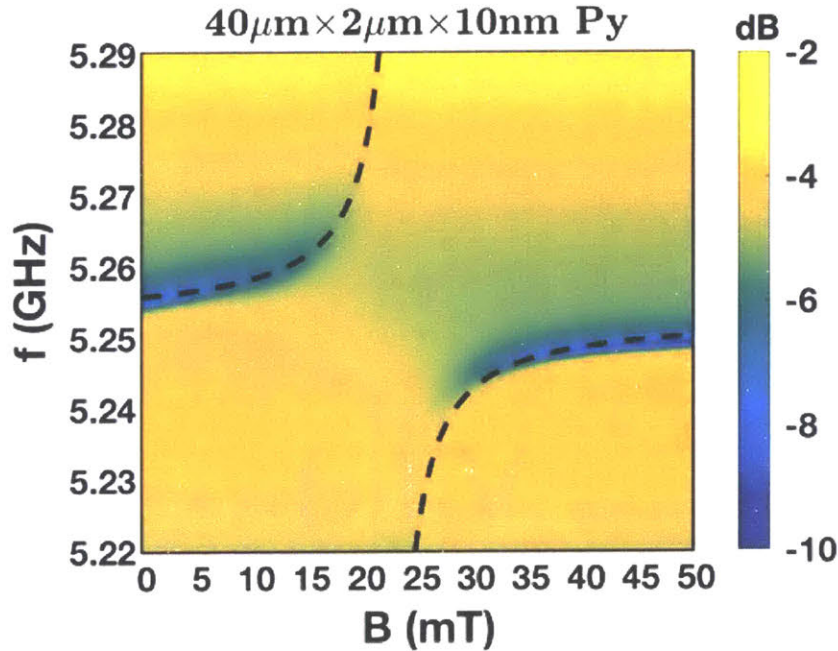


Figure 4-6: Microwave transmission as a function of frequency and in-plane magnetic field at 1.5 K. $\mu_0 M_s = 1.1$ T and $g/2\pi = 74.5$ MHz are determined from the fitting shown in dashed line. Minimum transmission shows up under resonant conditions.

Py size	f_{res} (GHz)	$\mu_0 M_s$ (T)	$g/2\pi$ (MHz)
$40\mu m \times 2\mu m$	5.2532	1.066	74.5
$20\mu m \times 2\mu m$	5.1955	1.083	49.8
$10\mu m \times 2\mu m$	5.1606	1.089	30.7

Table 4.2: Table for different lumped element resonators with Py 10 nm thick deposited.

devices with different length of Py stripes. The results are summarized in Table. 4.2. We note that large coupling strength can be achieved despite the small magnetic volume, compared with the CPW resonators.

4.5 Extraction of single spin-photon coupling strength

Here, we combine the data points in both CPW and LE resonators presented in Table. 4.1 and 4.2. The scaling of coupling strength as a function of magnetic volume (and spin number) is shown in Fig. 4-7. For both resonator designs, we confirm the scaling of $g \propto \sqrt{N}$ and extract the single spin coupling strength g_s .

For the CPW resonator design, $g_s^{\text{CPW}}/2\pi = 18$ Hz is obtained. As the Py stripe is at the center of the $20 \mu\text{m}$ wide signal line, we can assume that the RF magnetic field is uniform throughout the Py volume and estimate $b_{\text{rf}}^{\text{CPW}} = \mu_0/2w^{\text{CPW}}$. Together with the designed impedance $Z_r^{\text{CPW}} \approx 50 \Omega$ of CPW resonators, we calculate the theoretical g_s to be $g_{s,\text{theory}}^{\text{CPW}}/2\pi = 14$ Hz, which attains reasonable agreement with our experimental value. However, a more accurate theoretical value of impedance is given by $Z_r^{\text{CPW}} = Z_0\pi/2 \approx 78.5\Omega$, which will results in $g_{s,\text{theory}}^{\text{CPW}}/2\pi = 11.2$ Hz. Therefore, the experimental value is higher than the calculated theoretical value.

For the LE resonator design, we extract $g_s^{\text{LE}}/2\pi = 263$ Hz (Fig. ??), which is an order of magnitude larger than the value with CPW resonator. This allows another two orders of magnitude reduction in spin number N to achieve similar coupling strength. The $g_s^{\text{LE}}/2\pi$ value obtained in our experiment is larger than the one calculated using our model $g_{s,\text{theory}}^{\text{LE}}/2\pi = 141$ Hz, which can partially be attributed to the enhancement of magnetic field at the edge of the inductor wire due to the field's

nonuniform distribution [20, 10].

For both resonator designs, we note that the theoretical values of g_s always underestimate the experimental values. We should notice that in our theoretical derivation of the coupling strength g , the anisotropy effect is neglected and the circular precession of the magnon mode around the applied field direction is assumed. However, in the thin-film case, the precession orbit is actually elliptical, with the long axis lies in the device plane and parallel to the RF magnetic field generated by the inductive wire. Therefore, the overlapping of the precession orbit with the RF field will be increased due to the shape anisotropy, and the enhancement of the coupling strength is expected. The theoretical derivation is straightforward. However, in our experiment, most of the data points are not in the strong coupling regime due to the higher damping of the Py. It is known that the damping can result in renormalized coupling strength. Therefore, the careful comparison of the coupling strength between theory and experiment will be done in future experiment using magnetic material with lower

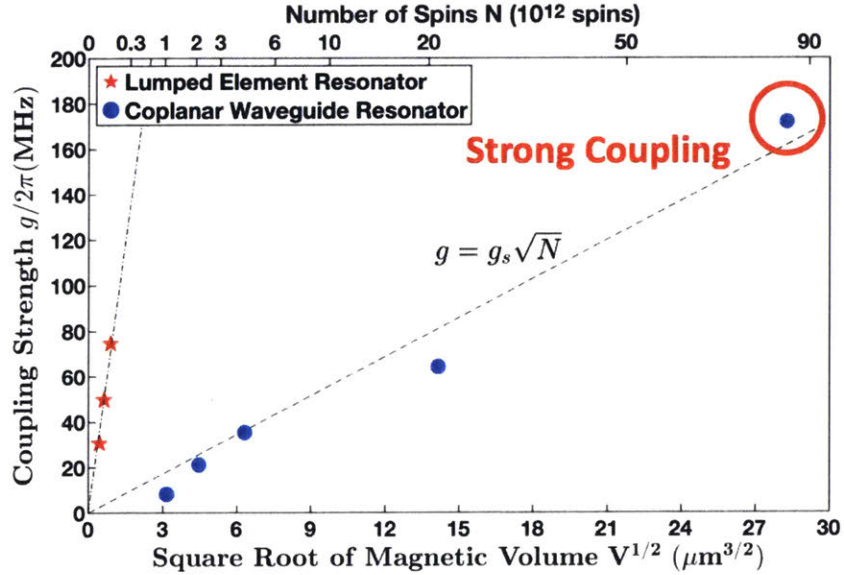


Figure 4-7: Magnon-photon coupling strength g as a function of magnetic volume and spin number. The dashed lines represent fittings of the scaling rule $g = g_s\sqrt{N}$. The single spin coupling strength for two resonators in this work are determined to be $g_s^{\text{CPW}}/2\pi = 18$ Hz and $g_s^{\text{LE}}/2\pi = 263$ Hz in CPW resonators and lumped element resonators, respectively.

damping, such as YIG.

In our study, with lithographically defined superconducting resonators and an on-chip coupled system design, we demonstrated an enhanced g_s compared with previous studies using 3D cavity with $g_s < 0.1$ Hz or flip-chip superconducting resonator design $g_s \approx 5$ Hz. With enhanced g_s , the number of spins N involved for reaching strong coupling is 3 orders of magnitude lower than previous experiments. In our experiment, a ferromagnetic metal with relatively high damping coefficient (Py) is employed. By simply replacing magnetic metals with insulator thin films with ultralow damping such as YIG ($Q > 1000$) [17], we expect strong magnon-photon coupling to be realized with as few as 10^7 spins using our current design. On the other hand, our studies show that the coupling strength obtained from the analytical model provides relatively precise estimate on the experimental values, which can be used as guidelines for further scaling down the magnonic system volume. For example, a LE resonator made by nanofabrication technique [27] with inductor width of ~ 100 nm (compared to $4\mu\text{m}$ in our current study) can further enhance g_s by a factor of 40 and reduce the number of spins for reaching strong coupling using YIG to 10^4 , which signify the potential for 12 orders of magnitude reduction in spin numbers compared with previous studies.

Chapter 5

Conclusions

In summary, we have demonstrated high cooperativity microwave photon-magnon coupling between a resonator mode in planar superconducting resonators and a Kittel mode in Py nanomagnets. Compared with previous literatures, we have made the following contributions:

1. Strong magnon-photon coupling with the smallest spin number N . With enhanced g_s , 3 orders of magnitude reduction in N is demonstrated. Moreover, another 9 orders of magnitude reduction is suggested with optimized material and resonator design.
2. The first demonstration of magnon-photon coupled systems utilizing metallic ferromagnets, which opens up the opportunities to investigate the coupled systems in a wide range of spintronic devices, such as magnetic tunnel junctions (MTJs).
3. The system is on-chip, lithographically scalable, realized using conventional Si-substrate, and Circuit QED compatible, which shows high potential for integrated hybrid quantum systems harnessing magnon physics.
4. The high coupling strength with nanomagnets opens up the possibility of electrical control of the hybrid system dynamics utilizing spintronic effects, such as spin torque and voltage controlled magnetic anisotropy.

Therefore, our works provide a novel platform of magnon-photon coupled systems, where the interplay of spintronics, light-matter interaction, and quantum information science can be studied in an on-chip and lithographically scalable architecture.[69]

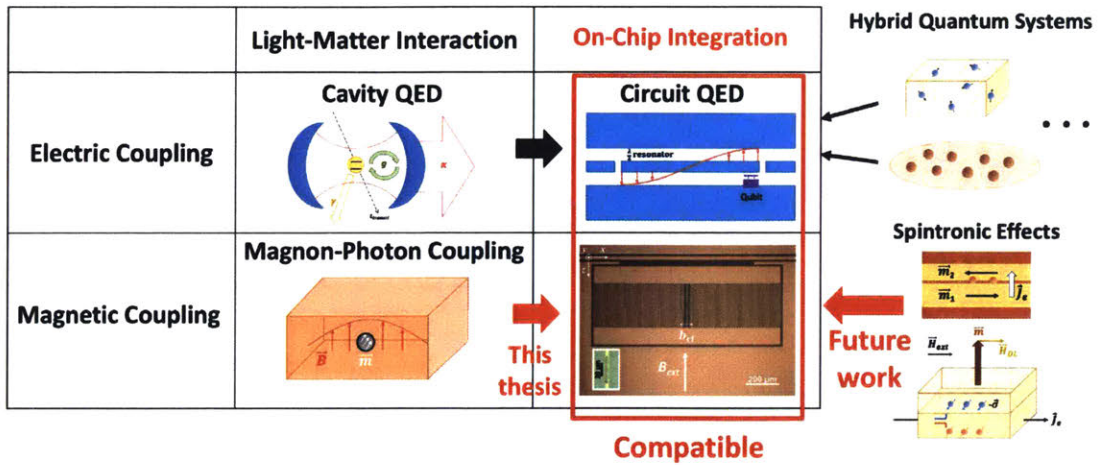


Figure 5-1: We developed the "Circuit QED version" of magnon-photon coupled systems, which provides potential applications to Hybrid Quantum Systems with magnon physics and spintronic effects.

Compared to previous studies of magnon-photon coupled systems, our results are similar to the development of Circuit QED from Cavity QED. Therefore, we may call our system "Magnon Circuit QED". The incorporation of spintronic effects will be the main focus of our future studies. Our contribution can be summarized in Fig. 5-1.

Bibliography

- [1] G. S. Agarwal. Vacuum-Field Rabi Splittings in Microwave Absorption by Rydberg Atoms in a Cavity. *Physical Review Letters*, 53(18):1732–1734, October 1984.
- [2] Pedram Khalili Amiri and Kang L. Wang. Voltage-controlled magnetic anisotropy in spintronic devices. *SPIN*, 02(03):1240002, September 2012.
- [3] R. AmsĀijss, Ch. Koller, T. NĀũbauer, S. Putz, S. Rotter, K. Sandner, S. Schneider, M. SchrambĀũck, G. Steinhauser, H. Ritsch, J. Schmiedmayer, and J. Majer. Cavity QED with Magnetically Coupled Collective Spin States. *Physical Review Letters*, 107(6):060502, August 2011.
- [4] K. Ando, S. Takahashi, K. Harii, K. Sasage, J. Ieda, S. Maekawa, and E. Saitoh. Electric Manipulation of Spin Relaxation Using the Spin Hall Effect. *Physical Review Letters*, 101(3):036601, July 2008.
- [5] A. AndrĀľ, D. DeMille, J. M. Doyle, M. D. Lukin, S. E. Maxwell, P. Rabl, R. J. Schoelkopf, and P. Zoller. A coherent all-electrical interface between polar molecules and mesoscopic superconducting resonators. *Nature Physics*, 2(9):636–642, September 2006.
- [6] Markus Aspelmeyer, Tobias J. Kippenberg, and Florian Marquardt. Cavity optomechanics. *Reviews of Modern Physics*, 86(4):1391–1452, December 2014.
- [7] Lihui Bai, M. Harder, Y.ĀľP. Chen, X. Fan, J.ĀľQ. Xiao, and C.-M. Hu. Spin Pumping in Electrodynamically Coupled Magnon-Photon Systems. *Physical Review Letters*, 114(22):227201, June 2015.
- [8] R. Barends, J. Kelly, A. Megrant, A. Veitia, D. Sank, E. Jeffrey, T. C. White, J. Mutus, A. G. Fowler, B. Campbell, Y. Chen, Z. Chen, B. Chiaro, A. Dunsworth, C. Neill, P. OĀľMalley, P. Roushan, A. Vainsencher, J. Wenner, A. N. Korotkov, A. N. Cleland, and John M. Martinis. Superconducting quantum circuits at the surface code threshold for fault tolerance. *Nature*, 508(7497):500–503, April 2014.
- [9] A. Bienfait, J. J. Pla, Y. Kubo, M. Stern, X. Zhou, C. C. Lo, C. D. Weis, T. Schenkel, M. L. W. Thewalt, D. Vion, D. Esteve, B. Julsgaard, K. MĀľlmer, J. J. L. Morton, and P. Bertet. Reaching the quantum limit of sensitivity in electron spin resonance. *Nature Nanotechnology*, 11(3):253–257, March 2016.

- [10] A. Bienfait, J. J. Pla, Y. Kubo, X. Zhou, M. Stern, C. C. Lo, C. D. Weis, T. Schenkel, D. Vion, D. Esteve, J. J. L. Morton, and P. Bertet. Controlling spin relaxation with a cavity. *Nature*, 531(7592):74–77, March 2016.
- [11] Alexandre Blais, Ren-Shou Huang, Andreas Wallraff, S. M. Girvin, and R. J. Schoelkopf. Cavity quantum electrodynamics for superconducting electrical circuits: An architecture for quantum computation. *Physical Review A*, 69(6):062320, June 2004.
- [12] Sergio Boixo, Sergei V. Isakov, Vadim N. Smelyanskiy, Ryan Babbush, Nan Ding, Zhang Jiang, Michael J. Bremner, John M. Martinis, and Hartmut Neven. Characterizing quantum supremacy in near-term devices. *Nature Physics*, 14(6):595–600, June 2018.
- [13] M. Brune, S. Haroche, V. Lefevre, J. M. Raimond, and N. Zagury. Quantum nondemolition measurement of small photon numbers by Rydberg-atom phase-sensitive detection. *Physical Review Letters*, 65(8):976–979, August 1990.
- [14] M. Brune, S. Haroche, J. M. Raimond, L. Davidovich, and N. Zagury. Manipulation of photons in a cavity by dispersive atom-field coupling: Quantum-nondemolition measurements and generation of “Schrödinger cat” states. *Physical Review A*, 45(7):5193–5214, April 1992.
- [15] M. Brune, F. Schmidt-Kaler, A. Maali, J. Dreyer, E. Hagley, J. M. Raimond, and S. Haroche. Quantum Rabi Oscillation: A Direct Test of Field Quantization in a Cavity. *Physical Review Letters*, 76(11):1800–1803, March 1996.
- [16] Iulia Buluta, Sahel Ashhab, and Franco Nori. Natural and artificial atoms for quantum computation. *Reports on Progress in Physics*, 74(10):104401, September 2011.
- [17] H. Chang, P. Li, W. Zhang, T. Liu, A. Hoffmann, L. Deng, and M. Wu. Nanometer-Thick Yttrium Iron Garnet Films With Extremely Low Damping. *IEEE Magnetics Letters*, 5:1–4, 2014.
- [18] Vladislav E. Demidov, Sergei Urazhdin, Henning Ulrichs, Vasyl Tiberkevich, Andrei Slavin, Dietmar Baither, Guido Schmitz, and Sergej O. Demokritov. Magnetic nano-oscillator driven by pure spin current. *Nature Materials*, 11(12):1028–1031, December 2012.
- [19] Zheng Duan, Andrew Smith, Liu Yang, Brian Youngblood, JÄirgen Lindner, Vladislav E. Demidov, Sergej O. Demokritov, and Ilya N. Krivorotov. Nanowire Spin Torque Oscillator Driven by Spin Orbit Torques. *Nature Communications*, 5:5616, December 2014. arXiv: 1404.7262.
- [20] C. Eichler, A. J. Sigillito, S. A. Lyon, and J. R. Petta. Electron Spin Resonance at the Level of 10^4 Spins Using Low Impedance Superconducting Resonators. *Physical Review Letters*, 118(3):037701, January 2017.

- [21] P. Forn-D̄az, L. Lamata, E. Rico, J. Kono, and E. Solano. Ultrastrong coupling regimes of light-matter interaction. *Reviews of Modern Physics*, 91(2):025005, June 2019.
- [22] Nicolas Gisin, Gr̄goire Ribordy, Wolfgang Tittel, and Hugo Zbinden. Quantum cryptography. *Reviews of Modern Physics*, 74(1):145–195, March 2002.
- [23] Maxim Goryachev, Warrick G. Farr, Daniel L. Creedon, Yaohui Fan, Mikhail Kostylev, and Michael E. Tobar. High-Cooperativity Cavity QED with Magnons at Microwave Frequencies. *Physical Review Applied*, 2(5):054002, November 2014.
- [24] P. Goy, J. M. Raimond, M. Gross, and S. Haroche. Observation of Cavity-Enhanced Single-Atom Spontaneous Emission. *Physical Review Letters*, 50(24):1903–1906, June 1983.
- [25] C. Grezes, B. Julsgaard, Y. Kubo, M. Stern, T. Umeda, J. Isoya, H. Sumiya, H. Abe, S. Onoda, T. Ohshima, V. Jacques, J. Esteve, D. Vion, D. Esteve, K. M̄ylmer, and P. Bertet. Multimode Storage and Retrieval of Microwave Fields in a Spin Ensemble. *Physical Review X*, 4(2):021049, June 2014.
- [26] M. Ḡuppl, A. Fragner, M. Baur, R. Bianchetti, S. Filipp, J. M. Fink, P. J. Leek, G. Puebla, L. Steffen, and A. Wallraff. Coplanar waveguide resonators for circuit quantum electrodynamics. *Journal of Applied Physics*, 104(11):113904, December 2008.
- [27] P. Haikka, Y. Kubo, A. Bienfait, P. Bertet, and K. M̄ylmer. Proposal for detecting a single electron spin in a microwave resonator. *Physical Review A*, 95(2):022306, February 2017.
- [28] M. Harder, Y. Yang, B. M̄. Yao, C. H. Yu, J. W. Rao, Y. S. Gui, R. L. Stamps, and C.-M. Hu. Level Attraction Due to Dissipative Magnon-Photon Coupling. *Physical Review Letters*, 121(13):137203, September 2018.
- [29] Michael Harder, Lihui Bai, Paul Hyde, and Can-Ming Hu. Topological properties of a coupled spin-photon system induced by damping. *Physical Review B*, 95(21):214411, June 2017.
- [30] Serge Haroche. Nobel Lecture: Controlling photons in a box and exploring the quantum to classical boundary. *Reviews of Modern Physics*, 85(3):1083–1102, July 2013.
- [31] C. J. Hood, M. S. Chapman, T. W. Lynn, and H. J. Kimble. Real-Time Cavity QED with Single Atoms. *Physical Review Letters*, 80(19):4157–4160, May 1998.
- [32] Hans Huebl, Christoph W. Zollitsch, Johannes Lotze, Fredrik Hocke, Moritz Greifenstein, Achim Marx, Rudolf Gross, and Sebastian T. B. Goennenwein. High Cooperativity in Coupled Microwave Resonator Ferrimagnetic Insulator Hybrids. *Physical Review Letters*, 111(12):127003, September 2013.

- [33] Rui Igreja and C. J. Dias. Analytical evaluation of the interdigital electrodes capacitance for a multi-layered structure. *Sensors and Actuators A: Physical*, 112(2):291–301, May 2004.
- [34] Atac Imamoglu. Cavity QED Based on Collective Magnetic Dipole Coupling: Spin Ensembles as Hybrid Two-Level Systems. *Physical Review Letters*, 102(8):083602, February 2009.
- [35] Kosuke Kakuyanagi, Yuichiro Matsuzaki, Corentin D’Almeida, Hiraku Toida, Kouichi Semba, Hiroshi Yamaguchi, William J. Munro, and Shiro Saito. Observation of Collective Coupling between an Engineered Ensemble of Macroscopic Artificial Atoms and a Superconducting Resonator. *Physical Review Letters*, 117(21):210503, November 2016.
- [36] J. Kelly, R. Barends, A. G. Fowler, A. Megrant, E. Jeffrey, T. C. White, D. Sank, J. Y. Mutus, B. Campbell, Yu Chen, Z. Chen, B. Chiaro, A. Dunsworth, I.-C. Hoi, C. Neill, P. J. J. O’Malley, C. Quintana, P. Roushan, A. Vainsencher, J. Wenner, A. N. Cleland, and John M. Martinis. State preservation by repetitive error detection in a superconducting quantum circuit. *Nature*, 519(7541):66–69, March 2015.
- [37] S. I. Kiselev, J. C. Sankey, I. N. Krivorotov, N. C. Emley, R. J. Schoelkopf, R. A. Buhrman, and D. C. Ralph. Microwave oscillations of a nanomagnet driven by a spin-polarized current. *Nature*, 425(6956):380–383, September 2003.
- [38] Daniel Kleppner. Inhibited Spontaneous Emission. *Physical Review Letters*, 47(4):233–236, July 1981.
- [39] Y. Kubo, C. Grezes, A. Dewes, T. Umeda, J. Isoya, H. Sumiya, N. Morishita, H. Abe, S. Onoda, T. Ohshima, V. Jacques, A. Drăgău, J.-F. Roch, I. Diniz, A. Auffeves, D. Vion, D. Esteve, and P. Bertet. Hybrid Quantum Circuit with a Superconducting Qubit Coupled to a Spin Ensemble. *Physical Review Letters*, 107(22):220501, November 2011.
- [40] Hitoshi Kubota, Akio Fukushima, Kay Yakushiji, Taro Nagahama, Shinji Yuasa, Koji Ando, Hiroki Maehara, Yoshinori Nagamine, Koji Tsunekawa, David D. Djayaprawira, Naoki Watanabe, and Yoshishige Suzuki. Quantitative measurement of voltage dependence of spin-transfer torque in MgO-based magnetic tunnel junctions. *Nature Physics*, 4(1):37–41, January 2008.
- [41] Gershon Kurizki, Patrice Bertet, Yuimaru Kubo, Klaus Mølmer, David Petrosyan, Peter Rabl, and Jürgen Schmiedmayer. Quantum technologies with hybrid systems. *Proceedings of the National Academy of Sciences*, 112(13):3866–3873, March 2015.
- [42] Dany Lachance-Quirion, Yutaka Tabuchi, Seiichiro Ishino, Atsushi Noguchi, Toyofumi Ishikawa, Rekishu Yamazaki, and Yasunobu Nakamura. Resolving quanta

- of collective spin excitations in a millimeter-sized ferromagnet. *Science Advances*, 3(7):e1603150, July 2017.
- [43] E. Lesne, Yu Fu, S. Oyarzun, J. C. Rojas-Sánchez, D. C. Vaz, H. Naganuma, G. Sicoli, J.-P. Attanali, M. Jamet, E. Jacquet, J.-M. George, A. Barthelmy, H. Jaffrès, A. Fert, M. Bibes, and L. Vila. Highly efficient and tunable spin-to-charge conversion through Rashba coupling at oxide interfaces. *Nature Materials*, 15(12):1261, December 2016.
- [44] Luqiao Liu, O. J. Lee, T. J. Gudmundsen, D. C. Ralph, and R. A. Buhrman. Current-Induced Switching of Perpendicularly Magnetized Magnetic Layers Using Spin Torque from the Spin Hall Effect. *Physical Review Letters*, 109(9):096602, August 2012.
- [45] Luqiao Liu, Takahiro Moriyama, D. C. Ralph, and R. A. Buhrman. Spin-Torque Ferromagnetic Resonance Induced by the Spin Hall Effect. *Physical Review Letters*, 106(3):036601, January 2011.
- [46] Luqiao Liu, Chi-Feng Pai, Y. Li, H. W. Tseng, D. C. Ralph, and R. A. Buhrman. Spin-Torque Switching with the Giant Spin Hall Effect of Tantalum. *Science*, 336(6081):555–558, May 2012.
- [47] Luqiao Liu, Chi-Feng Pai, D. C. Ralph, and R. A. Buhrman. Magnetic Oscillations Driven by the Spin Hall Effect in 3-Terminal Magnetic Tunnel Junction Devices. *Physical Review Letters*, 109(18):186602, October 2012.
- [48] X. Mi, M. Benito, S. Putz, D. M. Zajac, J. M. Taylor, Guido Burkard, and J. R. Petta. A coherent spin-photon interface in silicon. *Nature*, 555(7698):599–603, March 2018.
- [49] R. G. E. Morris, A. F. van Loo, S. Kosen, and A. D. Karenowska. Strong coupling of magnons in a YIG sphere to photons in a planar superconducting resonator in the quantum limit. *Scientific Reports*, 7(1):11511, September 2017.
- [50] O. Mosendz, J. E. Pearson, F. Y. Fradin, G. E. W. Bauer, S. D. Bader, and A. Hoffmann. Quantifying Spin Hall Angles from Spin Pumping: Experiments and Theory. *Physical Review Letters*, 104(4):046601, January 2010.
- [51] C. Neill, P. Roushan, K. Kechedzhi, S. Boixo, S. V. Isakov, V. Smelyanskiy, A. Megrant, B. Chiaro, A. Dunsworth, K. Arya, R. Barends, B. Burkett, Y. Chen, Z. Chen, A. Fowler, B. Foxen, M. Giustina, R. Graff, E. Jeffrey, T. Huang, J. Kelly, P. Klimov, E. Lucero, J. Mutus, M. Neeley, C. Quintana, D. Sank, A. Vainsencher, J. Wenner, T. C. White, H. Neven, and J. M. Martinis. A blueprint for demonstrating quantum supremacy with superconducting qubits. *Science*, 360(6385):195–199, April 2018.

- [52] A. Opremcak, I. V. Pechenezhskiy, C. Howington, B. G. Christensen, M. A. Beck, E. Leonard, J. Suttle, C. Wilen, K. N. Nesterov, G. J. Ribeill, T. Thorbeck, F. Schlenker, M. G. Vavilov, B. L. T. Plourde, and R. McDermott. Measurement of a superconducting qubit with a microwave photon counter. *Science*, 361(6408):1239–1242, September 2018.
- [53] K. Ounadjela, H. Lefakis, V. Speriosu, C. Hwang, and P. Alexopoulos. THICKNESS DEPENDENCE OF MAGNETIZATION AND MAGNETOSTRICTION OF NiFe AND NiFeRh FILMS. *Journal de Physique Colloques*, 49(C8):C8–1709–C8–1710, 1988.
- [54] K. D. Petersson, L. W. McFaul, M. D. Schroer, M. Jung, J. M. Taylor, A. A. Houck, and J. R. Petta. Circuit quantum electrodynamics with a spin qubit. *Nature*, 490(7420):380–383, October 2012.
- [55] Igor Proskurin, Rair MacÃlido, and Robert L. Stamps. Microscopic origin of level attraction for a coupled magnon-photon system in a microwave cavity. *arXiv:1904.11570 [cond-mat]*, April 2019. arXiv: 1904.11570.
- [56] P. Rabl, D. DeMille, J. M. Doyle, M. D. Lukin, R. J. Schoelkopf, and P. Zoller. Hybrid Quantum Processors: Molecular Ensembles as Quantum Memory for Solid State Circuits. *Physical Review Letters*, 97(3):033003, July 2006.
- [57] A. Rauschenbeutel, G. Nogues, S. Osnaghi, P. Bertet, M. Brune, J. M. Raimond, and S. Haroche. Coherent Operation of a Tunable Quantum Phase Gate in Cavity QED. *Physical Review Letters*, 83(24):5166–5169, December 1999.
- [58] Jack C. Sankey, Yong-Tao Cui, Jonathan Z. Sun, John C. Slonczewski, Robert A. Buhrman, and Daniel C. Ralph. Measurement of the spin-transfer-torque vector in magnetic tunnel junctions. *Nature Physics*, 4(1):67–71, January 2008.
- [59] R. J. Schoelkopf and S. M. Girvin. Wiring up quantum systems. *Nature*, 451(7179):664–669, February 2008.
- [60] D. I. Schuster, A. A. Houck, J. A. Schreier, A. Wallraff, J. M. Gambetta, A. Blais, L. Frunzio, J. Majer, B. Johnson, M. H. Devoret, S. M. Girvin, and R. J. Schoelkopf. Resolving photon number states in a superconducting circuit. *Nature*, 445(7127):515–518, February 2007.
- [61] D. I. Schuster, A. P. Sears, E. Ginossar, L. DiCarlo, L. Frunzio, J. J. L. Morton, H. Wu, G. A. D. Briggs, B. B. Buckley, D. D. Awschalom, and R. J. Schoelkopf. High-Cooperativity Coupling of Electron-Spin Ensembles to Superconducting Cavities. *Physical Review Letters*, 105(14):140501, September 2010.
- [62] Ã. O. Soykal and M. E. FlattÃl. Strong Field Interactions between a Nanomagnet and a Photonic Cavity. *Physical Review Letters*, 104(7):077202, February 2010.

- [63] C. P. Sun, L. F. Wei, Yu-xi Liu, and Franco Nori. Quantum transducers: Integrating transmission lines and nanomechanical resonators via charge qubits. *Physical Review A*, 73(2):022318, February 2006.
- [64] Yutaka Tabuchi, Seiichiro Ishino, Toyofumi Ishikawa, Rekishu Yamazaki, Koji Usami, and Yasunobu Nakamura. Hybridizing Ferromagnetic Magnons and Microwave Photons in the Quantum Limit. *Physical Review Letters*, 113(8):083603, August 2014.
- [65] Yutaka Tabuchi, Seiichiro Ishino, Atsushi Noguchi, Toyofumi Ishikawa, Rekishu Yamazaki, Koji Usami, and Yasunobu Nakamura. Coherent coupling between a ferromagnetic magnon and a superconducting qubit. *Science*, 349(6246):405–408, July 2015.
- [66] Yaroslav Tserkovnyak, Arne Brataas, and Gerrit E. W. Bauer. Enhanced Gilbert Damping in Thin Ferromagnetic Films. *Physical Review Letters*, 88(11):117601, February 2002.
- [67] Yaroslav Tserkovnyak, Arne Brataas, and Gerrit E. W. Bauer. Spin pumping and magnetization dynamics in metallic multilayers. *Physical Review B*, 66(22):224403, December 2002.
- [68] J. J. Viennot, M. C. Dartiailh, A. Cottet, and T. Kontos. Coherent coupling of a single spin to microwave cavity photons. *Science*, 349(6246):408–411, July 2015.
- [69] A. Wallraff, D. I. Schuster, A. Blais, L. Frunzio, R.-S. Huang, J. Majer, S. Kumar, S. M. Girvin, and R. J. Schoelkopf. Strong coupling of a single photon to a superconducting qubit using circuit quantum electrodynamics. *Nature*, 431(7005):162–167, September 2004.
- [70] Yi-Pu Wang, Guo-Qiang Zhang, Dengke Zhang, Tie-Fu Li, C.-M. Hu, and J. Q. You. Bistability of Cavity Magnon Polaritons. *Physical Review Letters*, 120(5):057202, January 2018.
- [71] G. Wendin. Quantum information processing with superconducting circuits: a review. *Reports on Progress in Physics*, 80(10):106001, September 2017.
- [72] David J. Wineland. Nobel Lecture: Superposition, entanglement, and raising Schrödinger’s cat. *Reviews of Modern Physics*, 85(3):1103–1114, July 2013.
- [73] Hua Wu, Richard E. George, Janus H. Wesenberg, Klaus M. Aylmer, David I. Schuster, Robert J. Schoelkopf, Kohei M. Itoh, Arzhang Ardavan, John J. L. Morton, and G. Andrew D. Briggs. Storage of Multiple Coherent Microwave Excitations in an Electron Spin Ensemble. *Physical Review Letters*, 105(14):140503, September 2010.
- [74] Ze-Liang Xiang, Sahel Ashhab, J. Q. You, and Franco Nori. Hybrid quantum circuits: Superconducting circuits interacting with other quantum systems. *Reviews of Modern Physics*, 85(2):623–653, April 2013.

- [75] Dengke Zhang, J. Q. You, Tie-Fu Li, Xiao-Qing Luo, and Yi-Pu Wang. Observation of the exceptional point in cavity magnon-polaritons. *Nature Communications*, 8(1):1368, December 2017.
- [76] Xufeng Zhang, Chang-Ling Zou, Liang Jiang, and Hong X. Tang. Strongly Coupled Magnons and Cavity Microwave Photons. *Physical Review Letters*, 113(15):156401, October 2014.
- [77] Xufeng Zhang, Chang-Ling Zou, Na Zhu, Florian Marquardt, Liang Jiang, and Hong X. Tang. Magnon dark modes and gradient memory. *Nature Communications*, 6:ncomms9914, November 2015.
- [78] Xiaobo Zhu, Shiro Saito, Alexander Kemp, Kosuke Kakuyanagi, Shin-ichi Karimoto, Hayato Nakano, William J. Munro, Yasuhiro Tokura, Mark S. Everitt, Kae Nemoto, Makoto Kasu, Norikazu Mizuochi, and Kouichi Semba. Coherent coupling of a superconducting flux qubit to an electron spin ensemble in diamond. *Nature*, 478(7368):221–224, October 2011.